LAWRENCE
LIVERMORE
NATIONAL
LABORATORY

High-Energy Neutron Imaging Development at LLNL

J. M. Hall (PI), B. Rusnak (PE), S. Shen and P. J. Fitsos

Lawrence Livermore National Laboratory

5 January 2006

Disclaimer

This document was prepared as an account of work sponsored by an agency of the United States Government. Neither the United States Government nor the University of California nor any of their employees, makes any warranty, express or implied, or assumes any legal liability or responsibility for the accuracy, completeness, or usefulness of any information, apparatus, product, or process disclosed, or represents that its use would not infringe privately owned rights. Reference herein to any specific commercial product, process, or service by trade name, trademark, manufacturer, or otherwise, does not necessarily constitute or imply its endorsement, recommendation, or favoring by the United States Government or the University of California. The views and opinions of authors expressed herein do not necessarily state or reflect those of the United States Government or the University of California, and shall not be used for advertising or product endorsement purposes.

Auspices Statement

This work was performed under the auspices of the U. S. Department of Energy (DOE) by the University of California, Lawrence Livermore National Laboratory (LLNL) under Contract No. W-7405-Eng-48.

High-Energy Neutron Imaging Development at LLNL

James Hall (PI), Brian Rusnak (PE), Stewart Shen and Peter Fitsos

Lawrence Livermore National Laboratory, P.O. Box 808, M/S L-050, Livermore, CA 94551-9900

Abstract We are proceeding with the development of a high-energy (10 MeV) neutron imaging system for use as an inspection tool in nuclear stockpile stewardship applications. Our goal is to develop and deploy an imaging system capable of detecting cubic-mm-scale voids, cracks or other significant structural defects in heavily-shielded low-Z materials within nuclear device components. The final production-line system will be relatively compact (suitable for use in existing or proposed facilities within the DOE complex) and capable of acquiring both radiographic and tomographic (CT) images. In this report, we will review our programmatic accomplishments to date, focusing primarily on progress made during FY05. The design status of the high-intensity, accelerator-driven neutron source and large-format imaging detector associated with the system will be discussed and results from a recent series of high-energy neutron imaging experiments conducted at the Ohio University Accelerator Laboratory (OUAL) will also be presented.

INTRODUCTION

We are proceeding with the development of a high-energy (10 MeV) neutron imaging system for use as an inspection tool in nuclear stockpile stewardship applications associated with the DOE Enhanced Surveillance Campaign (ESC). Our goal is to develop and deploy an imaging system capable of detecting cubic-mm-scale voids, cracks or other significant structural defects in heavily-shielded low-Z materials within nuclear device components. Potential applications for this new diagnostic include: (1) collection of "baseline" data characterizing the "as-designed" vs. "as-built" configurations of stockpiled systems (relevant to ESC programs), (2) routine surveillance of stockpiled systems (relevant to Directed Stockpile Work (DSW)), (3) inspection and/or re-certification of nuclear device components (relevant to Stockpile Lifetime Extension Programs (SLEPs)), (4) non-destructive damage assessment (relevant to Stockpile-to-Target Sequence (STS) engineering tests) and (5) identification of specific units for potential stockpile reductions if mandated. Note that our intent is to develop an inspection system that will *complement* - not replace - existing ESC x-ray diagnostic tools.

The final production-line imaging system will be relatively compact (suitable for use in existing or proposed facilities within the DOE complex) and capable of acquiring both radiographic and tomographic (CT) images. It will consist of an intense, accelerator-driven D(d,n)^{3}He neutron source ($E_n \approx 10$ MeV @ 0°) with an effective yield of $\approx 10^{11}$ n/sec/sr along the beam axis and an effective focal spot size of ≈ 1.50 mm (FWHM), a multi-axis staging system to support and manipulate objects under inspection and a neutron imaging detector (*cf.* Figure 1). The detector itself will consist of a transparent plastic scintillator (*e.g.* BC-408) viewed indirectly by one or more high-resolution CCD cameras. The ultimate spatial resolution of the imaging system will, of course, depend on the details of the final design and implementation, but it is expected to be ≤ 1.00 mm (FWHM) at the object position.

The conceptual design of the proposed imaging system and results from a number of previous imaging experiments have already been published in the open literature [1 - 6] and summarized in prior ESC annual reports. In this report, we will review our programmatic accomplishments to date, focusing primarily on progress made during FY05. The design status of the high-intensity, accelerator-driven neutron source and large-format imaging detector associated with the system will be discussed and results from a recent series of high-energy neutron imaging experiments conducted at the Ohio University Accelerator Laboratory (OUAL) in Athens, OH, will also be presented.

SOURCE DEVELOPMENT

The development of an intense, high-energy neutron source suitable for use in a full-scale, production-line imaging system is critical to the success of this project. As noted above, we propose to use an accelerator-driven D(d,n)^{3}He neutron source operating at ≈ 10 MeV. In order to meet our performance requirements, the source will need to have an effective yield of $\approx 10^{11}$ n/sec/sr along the beam axis and an effective focal spot size of ≈ 1.50 mm (FWHM). While this is certainly achievable using existing (*i.e.* commercial and low-risk) technologies, it does pose some challenging technical problems, particularly in the design of the D_2 gas target endstation and residual beam stop.

Accelerator Design

The accelerator system that we propose to use in our full-scale neutron source will be based on mature, commercially-available technology. It will consist of a

D$^+$ ion source and a pair of compact radio-frequency quadrupoles (RFQs) coupled to a short drift-tube linac (DTL) (*cf*. Figure 2). The system must accelerate D$^+$ ions to an energy of $\approx$ 7 MeV and be capable of delivering an average ion current of $\approx$ 320 μA to a D$_2$ gas cell located in the target endstation in order to generate a neutron yield sufficient for our proposed imaging applications. The beam pulse frequency will need to be $\approx$ 140 Hz in order to enable coupling with the endstation and the duty factor should be $\approx$ 1.95% (this implies a peak current of $\approx$ 15 - 17 mA and a pulse width of $\approx$ 139 μsec). The overall emittance ($\varepsilon_{x,y}$) of the beam must also be $\leq$ 3.3 mm-mrad in order to achieve the small focal spot size required at the endstation.

The full-up design for this accelerator system was completed during Q4 of FY02 by the proposed vendor, AccSys Technologies, Inc. of Pleasanton, CA, under a sole-source contract from LLNL. The design was subsequently reviewed and accepted by our PE during Q1 of FY03. The projected cost of the system at that time was $\approx$ \$2.5M (now estimated at $\approx$ \$2.9M due to inflation) and the estimated lead time for fabrication and delivery was $\approx$ 12 - 18 months [7].

HEBT System

The initial (conceptual) design of the high-energy beam transport (HEBT) system needed to transport and focus D$^+$ ions from the accelerator into the target endstation was developed using the charged particle transport code TRACE3D during Q1 of FY03 (*cf*. Figure 3); however, based on guidance from ESC management at LLNL, we have elected to focus our effort and available funding since that time on the development of other system components involving relatively higher technical risk and/or longer lead times. Finalizing the design of the HEBT system (*i.e.* identifying specific, commercially-available focusing elements compatible with our beam transport requirements and then integrating them into the overall system design) is not expected to be a particularly challenging problem. Depending on project funding and ESC priorities, we would hope to complete this task sometime in FY06.

Endstation Design

The simultaneous requirements for a large D$^+$ ion current and relatively small focal spot size imposed by our proposed imaging applications effectively preclude the use of a conventional (*i.e.* "windowed") D$_2$ gas cell in the target endstation due to the fact that there simply exist no window materials capable of handling the relatively large areal power densities anticipated ($\approx$ 125 kW/cm^2 (average) in our case); therefore, we have focused our effort on the development of "windowless" D$_2$ gas cell designs which can be incorporated into the

endstation and coupled to our pulsed accelerator system for use as an intense neutron source.

The most promising way to handle the large areal power densities anticipated with this source appears to be through the use of a "rotating-aperture" (RA) gas cell. In this approach, narrow ($\approx$ 4 - 5 mm diameter) entrance and exit apertures on the high-pressure ($\approx$ 3 atma) gas cell and any adjacent differential pumping stages are "open" only when they coincide with matching apertures in a series of rotating disks synchronized to the pulse frequency of the accelerator beam. This effectively isolates the high-pressure gas in the cell from the accelerator vacuum system. Pioneering research conducted at MIT [8 - 11] has demonstrated that even a rudimentary RA system can create a very effective "plug" between a pressurized gas cell and a differential pumping system and work done at the DeBeers Diamond Research Laboratory in South Africa [12] has since proven the effectiveness of these systems in production-line applications.

Our initial RA target endstation design was based on a contained, "turbulent-volume" approach similar to that used in the early work at MIT (*cf*. Figure 4). The rotating apertures were immersed in the high-pressure D$_2$ target gas in this design in order to facilitate sealing and minimize pressure-induced pulsing of the rotors. It was thought at the time that placing the rotors inside the cell would also induce turbulent mixing in the gas and thereby improve convective cooling.

While this approach initially seemed to be a viable way to contain the high-pressure D$_2$ gas, there were still concerns that even the combination of turbulent mixing and convective cooling would be insufficient to prevent density rarefactions in the target gas due to beam heating ("burn through"). Subsequent fluid hydrodynamics calculations done with LLNL's ALE3D code indicated that this was, in fact, the case. For peak beam currents in the 5 - 20 mA range, significant heating of the target gas was found to occur within 10's of μsec, causing a rapid drop in density along the beam channel (*cf*. Figure 5) and an attendant decrease in the neutron yield that one might normally expect for a given incident beam current and gas cell pressure (*cf*. Figure 6).

Following a formal Engineering Design Review of this system conducted at LLNL during Q3 of FY02, we revised the design of the target endstation to incorporate a means to rapidly refresh the beam channel with cool D$_2$ gas at the required density in an effort to mitigate beam heating effects. Our current, single-stage design features a cross-flow D$_2$ venturi capped at either end by baffled, rotating apertures (*cf*. Figure 7). If the venturi is designed to generate a sufficiently high flow rate (*e.g.* $\approx$ 200 - 400 m/s), the D$_2$ gas in the beam channel ($\approx$ 1.50 mm FWHM) can be effectively refreshed $\geq$ 20 times during the course of a single beam pulse ($\approx$ 139 μsec). Additional ALE3D calculations done during FY04 con-

firmed that it should be possible to maintain a D_2 gas density in the beam channel equivalent to an average pressure of ≈ 3 atma using reasonably-sized, commercially-available vacuum pumps and standard gas handling systems (*cf.* Figure 8). This, in turn, should allow us to maintain a neutron yield from the source that is very close to the required level (*cf.* Figure 9).

The basic design of the new cross-flow D_2 venturi endstation was actually completed during Q1 of FY03; however, unanticipated ESC budget shortfalls during FY03 prevented us from finalizing the design that year. With restored funding, the final design package was quickly completed during Q1 of FY04 and two full-scale prototypes of the endstation suitable for use in pressure testing were subsequently fabricated by a precision machine shop, the CHAMP Company of Campbell, CA, under a sole-source contract from LLNL. The first of these units was delivered at the end of Q3 of FY04 (*cf.* Figure 10) and installed in a custom-designed vacuum enclosure equipped with a variety of sensors for diagnostic purposes (*cf.* Figure 11).

One of the primary goals in designing and fabricating these initial test units was to verify that we could achieve a gap spacing of ≤ 0.002" between a high-speed rotor and stator (*i.e.* the venturi in our case). The width of the gap will be a critical factor in mitigating leak rates from the high-pressure gas cell and maintaining a base pressure as low as possible in the endstation. In order to facilitate making these gap measurements, the venturi that would normally be used in an actual production unit was replaced by a rectangular cross-flow tube with a straight throat which could be used in tests with static gas (*cf.* Figure 12). The opposing surfaces of the rotors and cross-flow tube were all hard anodized with alumina, allowing them to be lapped and then precision ground for smoothness and flatness.

We began conduction performance tests on the first of these units in Q4 of FY04, following a previously-devised test plan, and quickly verified that the rotating machinery part of the assembly worked as intended in vacuum; however, we suffered a minor setback when first trying to run the cross-flow tube at high pressure. Shortly after the tube was pressurized with He gas at ≈ 3 atma (used as a surrogate for D_2 for safety reasons) and brought up to operational speeds (≈ 1000 RPM), residual deposits of hardened alumina "mud" that had apparently accumulated in the baffles of the rotors during the original surface grinding process (and defied our efforts to clean them out) broke loose due to pressure pulsing and caused the upstream rotor to seize. As a result, we decided to temporarily replace the baffled rotors with solid rotor assemblies with simple through holes for apertures. The new rotors worked very well and allowed us to proceed with our high pressure tests of the system during Q2 and Q3 of FY05 without any further difficulties.

A series of measurements done using both optical and RF resonance techniques established that the gap between the high-speed rotors and stators in our prototype RA assembly could, indeed, be held to ≤ 0.002", even when the system was run at high gas pressure (≥ 3 atma). Two different series of high pressure tests were run, each covering a range of $\approx 0.125 - 3.150$ atma. In the first series, the rotors were held fixed with the apertures misaligned (closed). Gas leakage was limited to the narrow gap between the rotors and stators in this case and was measured to be < 16 Torr when the cross-flow tube was pressurized to ≈ 3 atma (*cf.* Figure 13). In the second series of tests, the rotors were run at a typical operating speed (≈ 1000 RPM). The overall leak rate in this case was measured to be < 75 Torr when the cross-flow tube was pressurized to ≈ 3 atma (*cf.* Figure 14). While these base pressures were not quite as low as we would like in a production line unit (*i.e.* < 10 Torr), the results were nonetheless encouraging.

Based on our experience gained in assembling and testing these initial RA units and drawing upon the expertise of our new precision engineer (P. Fitsos), we developed a conceptual design for a 3rd generation RA system during Q4 of FY05 (*cf.* Figure 15). This system will use the same drive motor and mounting scheme as our initial RA units, but it will include high-tolerance thrust bearings integrated directly into the block which houses the high-pressure venturi cross-flow tube. We believe that this will allow us to maintain a gap spacing of < 0.001" between the rotors and stators and an overall base pressure in the endstation of < 10 Torr, even when the system is run at high gas pressure (≥ 3 atma). We are ready to proceed with the final design and fabrication of this new system (along with the high-pressure gas handling system needed to run performance tests with the cross-flow venturi in place) at any time; however, actual progress on these tasks will be contingent on FY06 funding levels for this project.

The laboratory research activities described in this section were carried out under the auspices of an approved Integrated Work Sheet (LLNL IWS # 11618, *Prototype Rotating Aperture System*, RI: P. Fitsos) and in accordance with a specific Engineering Safety Note and all applicable LLNL facility Operating Safety Procedures. Copies of these documents and/or additional information on personnel safety issues related to this work may be obtained directly from the authors of this report upon request.

Beam Stop

After the incident D^+ ion beam passes through the D_2 gas cell in the endstation, its energy needs to be dissipated in a way that not only has minimal impact on the intensity and spatial distribution of the primary (quasi-monoenergetic) neutron beam generated in the

gas cell, but which also produces as few additional (broad-spectrum) neutrons as possible. We recognize that the design of a suitable beam stop poses a significant technical challenge and two different approaches to the problem were investigated during FY05, each with inherent advantages and disadvantages.

The first approach considered involved dissipating the beam energy in a conventional solid beam stop fabricated from a high-Z refractive metal (*e.g*. W). While this would seem to be the most straight-forward approach from a purely mechanical perspective, extensive energy deposition and analytical heat flow calculations done on both "grazing incidence" and "suspended nipple" type beam stop designs indicated that the incident beam energy could not be dissipated without resorting to the use of materials so thick that they would almost certainly have a significant (negative) impact on the intensity and spatial distribution of the primary neutron beam. Additional problems posed by deuterium implanted in the beam stop and operational safety issues (*e.g*. the potential for spontaneous D_2 combustion in the advent of a vacuum failure) have lead us to shelve this approach for the time being.

The second approach considered – and our current focus - involves dumping the residual beam into a high-pressure ($\approx$ 3 atma), high-Z gas such as Ar or Xe located in a cell immediately downstream from the D_2 gas cell. The incident beam power ($\approx$ 2.24 kW (average) in our case) could then be removed by using a heat exchanger in the high-Z gas recirculation loop. Our preliminary calculations indicate that a two stage rotating aperture located at the exit of the target gas cell will serve to minimize mixing between the two gases and the purity of the different gas streams can potentially be maintained by using a gas handling system that exploits differences in the thermodynamic transport properties of the gases. High-pressure Ar or Xe gas should have essentially no impact on either the intensity or the spatial distribution of the primary neutron beam and beam breakup measurements for D^+ ions incident on Ar and Xe gas have shown that neither produces a significant number of additional (broad-spectrum) neutrons; however, additional fluid hydrodynamics calculations similar to those done for the D_2 gas cell are currently being done to ensure that beam burn through in the stopping gas and turbulent mixing between the target and stopping gases will not be problems.

IMAGING DETECTOR

The development of a high-efficiency, large-format neutron detector suitable for use in a full-scale, production-line imaging system is also critical to the success of this project. While the prototype detector developed for use in our experiments at OUAL has worked quite well thus far, allowing us to validate the potential of neutron imaging by capturing radiographic and tomographic images of a variety of test objects, its format is only $\approx$ 30 cm X 30 cm. The full-scale detector that we envision will need to have a format $\approx$ 2 - 3 times this size in order to meet the requirements of potential ESC inspection scenarios. As noted above, the detector will consist of a plastic scintillator (*e.g*. BC-408) viewed indirectly by one or more high-resolution CCD cameras. The ultimate spatial resolution of the imaging system will depend on the details of the final design and implementation, but it is expected to be $\leq$ 1.00 mm (FWHM) at the object position. While not as good as some x-ray imaging systems, this is thought to be adequate for most proposed ESC applications.

A preliminary design study related to the development of the full-scale imaging detector was completed during Q4 of FY04 by the proposed vendor, Optics1, Inc. of Westlake Village, CA, under a sole-source contract from LLNL. This study focused on two different design options (*cf*. Figure 16) and involved identifying suitable sensors, designing fast optical lens systems and defining predicted resolutions and photon error budgets (*i.e*. signal-to-noise (S/N) ratios) for each case.

Design option 1 utilizes an array of four overlapping 2048 X 2048, 24 μm pixel, TE-cooled, CCD cameras to image an 85 cm X 85 cm field-of-view at the scintillator. This design is similar to that recently built by Optics1 for use in an ESC high-resolution x-ray imaging system for use at Pantex and would allow us to image objects of interest at a geometrical magnification factor of $\approx$ 2:1 (which minimizes image noise caused by internal scattering within the object). Image registration would be done using a dedicated control computer with final processing and analysis being done off-line in a secure environment. The predicted S/N ratio for this design option is $\approx$ 1.3X that of our current prototype imaging detector at OUAL.

Design option 2 utilizes a single 4096 X 4096, 15 μm pixel, TE-cooled, CCD camera to image a 65 cm X 65 cm field-of-view at the scintillator. This design is larger in scale but conceptually similar to that currently being used in our imaging experiments at OUAL and should provide optical resolution comparable to that of option 1; however, its somewhat smaller field-of-view will require us to image at a geometrical magnification factor of $\approx$ 1.25:1 instead of 2:1. While this might result in a slight increase in image noise due to internal scattering within the object, it should also decrease the projected source spot size at the image plane, thereby allowing us to push the ultimate spatial resolution at the object position below 1.00 mm (FWHM). The predicted S/N ratio for this design is $\approx$ 82X that of our current prototype imaging detector at OUAL. Due to its inherent simplicity, lower cost and higher predicted performance, this option is our current favorite. We issued a sole-source contract to Optics1 to design and fabricate

the lens for this system during Q4 of FY05 and expect to take delivery by late FY06; however, procurement of the CCD camera and the final fabrication of a full-scale prototype of this detector (*cf*. Figure 17) will, again, be contingent on FY06 funding levels.

RECENT EXPERIMENTS

We conducted one series of experiments at OUAL during Q2 of FY05, during which three different unclassified test objects with features of interest to current Pantex or ESC programs were tomographically imaged with high-energy neutrons.

The basic setup of the experiments was similar to that described in previous reports. A nearly monoenergetic, 10 MeV neutron beam was generated by focussing 6.85 MeV D^+ ions extracted from OUAL's tandem van de Graaff accelerator into a cylindrical D_2 gas cell, 1 cm in diameter and 8 cm long, attached to the end of a beam line. The gas cell was capped with a thin ($\approx 5~\mu$m) W entrance window and maintained at a static pressure of ≈ 45 psia (≈ 3 atma). The average D^+ ion current at the gas cell was $\approx 8.5~\mu$A during each of the imaging runs. This corresponds to an estimated 10 MeV neutron yield of $\approx 5.6 \times 10^9$ n/sec/sr along the beam axis (*i.e.* $\approx 1/20^{th}$ of the intensity of the source proposed for our full-scale system). The effective focal spot size of the beam was ≈ 3 mm (FWHM) at the entrance window to the gas cell (*i.e.* $\approx 2X$ that of the source proposed for our full-scale system). The test objects were placed on a rotation stage ≈ 200 cm from the neutron source and ≈ 200 cm from the imaging detector, resulting in a geometric magnification factor of $\approx 2:1$ at the image plane. The imaging detector consisted of a 30 cm X 30 cm X 4 cm thick BC-408 transparent plastic scintillator viewed indirectly by a single high-resolution (1024 X 1024; 24 μm pixel), LN_2-cooled, CCD camera with a high-speed (f/1.0) commercial photographic lens.

Tomographic (CT) imaging of the test objects was facilitated using a high-precision, computer-controlled rotation stage interfaced to our existing data acquisition system at OUAL. The control system (driven using a simple LabView script) is fully automated, virtually immune to neutron source faults (*i.e.* temporary or even long-term loss of beam) and capable of taking CT data sets consisting of 4, 8, 16, 32, 64, 128, *etc*. interleaved images of an object at equally spaced angular intervals distributed over a 360° rotation.

The first test object imaged in this series was designed and built by weapons engineers at the DOE Pantex Plant and had previously been imaged at OUAL in FY04. It consisted of a stack of three PBX-9502 IHE samples uniformly pressed to different densities within a relatively narrow range (≈ 1.84, 1.87 and 1.90 g/cc) and joined together to form a single 2.00" high annular cylinder with a 2.00" OD and 0.375" ID. The IHE stack

was shielded by a 0.125" thick high-Z (U6%Nb) clamshell and had a low-Z (Be) sleeve with a 0.125" wall thickness inserted along its centerline (*cf*. Figure 18). A 0.050" thick Silastic pad with an array of eight holes ranging in diameter from 1.00" down to 1/64" was also sandwiched in between the U6%Nb clamshell and the IHE (just visible in the photo in Figure 18). The final assembly was mounted on a low-mass aluminum stand securely attached to the rotation stage and imaged perpendicular to its principal axis.

The full CT data set in this case consisted of a series of 256 20 minute exposures taken over a 360° rotation ($\Delta = 1.4063°$) (the FY04 study involving this test object was limited to only 128 images due to scheduling constraints and mechanical problems at OUAL). The individual images were of good quality (*cf*. Figure 19) and revealed the basic structure of the test object. The CT data set was processed using LLNL's Constrained Conjugate Gradient (CCG) cone-beam reconstruction algorithm, a portion of the development of which has been funded by this project. The CCG algorithm utilizes an iterative, constrained (*e.g.* $\mu X \geq 0$) least-squares fitting procedure which, while somewhat more CPU intensive (*i.e.* slower) than Conventional Back Projection (CBP) algorithms, has been shown to significantly reduce overall statistical noise levels in CT reconstructions (*cf*. Figure 20).

Horizontal and vertical slices taken through CT reconstructions of the Pantex test object again revealed its basic structure, including material contours and even the bond joints between the three IHE segments (*cf*. Figure 21); however, in spite of increasing the number of images of the object taken during this run, the small density differences between the IHE segments (≈ 0.03 g/cc) and the holes in the 0.050" Silastic pad were still not clearly discernable in the reconstructions (*cf*. Figure 22). While we were able to discern (and even quantify) IHE density differences as small as 0.05 g/cc and holes in shielded Silastic padding $\geq 1/8$" in diameter in radiographic images of other test objects taken at OUAL during FY03, the detailed structure of this particular object may be beyond the limits of what we can reasonably expect to see with our prototype imaging detector and the neutron source at OUAL.

The second test object imaged in this series was originally designed and built at LLNL for use in tomographic neutron imaging experiments at OUAL; however, it was subsequently modified by LLNL's ESC x-ray imaging team and recently used in a comparative study of 9 MeV and 15 MeV e-Bremsstrahlung imaging systems conducted at LLNL and Hill AFB, respectively [13]. As imaged, the object consisted of a 4.00" high, 2.00" diameter polyethylene cylinder shielded by a 1.00" thick lead shell and a 0.50" thick aluminum sleeve (*cf*. Figure 23). The poly cylinder actually consisted of two "half cylinders" with a series of 11 holes

ranging in diameter from 10.00 mm down to ≈ 0.40 mm machined into the inner (flat) surface of one half and the outer (curved) surface of the other. The maximum value of ρx for this object (measured along the inner radius of the Pb shell) was estimated to be ≈ 107 gm/cm^2. The final assembly was again mounted on a low-mass aluminum stand attached to the rotation stage and imaged perpendicular to its principal axis.

The full neutron CT data set in this case consisted of a series of 128 20 minute exposures taken over a 360° rotation ($\Delta = 2.8125°$). The 9 MeV x-ray CT data (presented here for comparison) consisted of a series of 900 exposures taken over a 360° rotation ($\Delta = 0.4000°$). The neutron CT data set was again processed using the CCG cone-beam reconstruction algorithm, while the x-ray CT reconstructions were done using a CBP algorithm to expedite processing.

Individual radiographic images extracted from the 10 MeV neutron and 9 MeV x-ray CT data sets at similar viewing angles (0°) each revealed the basic structure of the test object (*cf.* Figure 24); however, the neutron images showed significantly higher contrast and revealed much greater structural detail than did the x-ray images. The shell structure of the test object and voids in the poly cylinder as small as ≈ 1.25 mm in diameter were clearly discernable in vertical slices taken at 0° through the neutron CT reconstruction (*cf.* Figure 25). The larger voids (≥ 1.25 mm diameter) near the center of the poly cylinder were also clearly discernable in vertical slices taken at 90° through both the neutron and x-ray CT reconstructions (*cf.* Figure 26); however, the neutron images again showed much higher contrast, allowing the full structure of the test object (*e.g.* voids *and* inner surface contours) to be viewed at a single contrast setting. Horizontal slices taken through the neutron CT reconstruction at various elevations clearly reveled not only the void structures in the test object, but also the narrow ($\leq 0.005"$) "contact gap" between the two halves of the poly cylinder (*cf.* Figure 27). The void structures and contact gap were also discernable in the x-ray CT reconstruction, although (again) at *much* lower contrast (*cf.* Figure 28).

The third and final test object imaged in this series was designed and built at LLNL to simulate voids and metal hydride formations at high-Z/low-Z interfaces. It consisted of a 3.00" high, 1.50" diameter polyethylene cylinder shielded by a 1.25" thick tungsten shell (*cf.* Figure 29). Sets of right-circular holes 1.00, 2.00, 3.00 and 4.00 mm in diameter (with corresponding depths) were machined into the inner contour of the W shell at its midplane and the outer contour of the poly cylinder 0.50" above and below its midplane. The holes in the W shell and the lower set of holes in the poly cylinder were then filled with mercury amalgam (dental filling) at a nominal density of ≈ 10.5 g/cc to simulate metal hydride formations. The maximum value of ρx for this object (measured along the inner radius of the W shell) was estimated to be ≈ 182 gm/cm^2. As before, the final assembly was mounted on a low-mass aluminum stand attached to the rotation stage and imaged perpendicular to its principal axis.

The full CT data set in this case was limited to a series of only 64 20 minute exposures taken over a 360° rotation ($\Delta = 5.6250°$) due to scheduling conflicts at OUAL. The CT data set was again processed using the CCG cone-beam reconstruction algorithm.

Vertical slices through the CT reconstruction of the test object clearly revealed the 4.00 mm (50.3 mm^3) and 3.00 mm (21.2 mm^3) voids and simulated hydride formations in both the poly cylinder and the W shell (*cf.* Figure 30); however, neither the 2.00 mm (6.28 mm^3) nor the 1.00 mm (0.79 mm^3) features were discernable in the reconstruction (*cf.* Figure 31) due to inadequate angular resolution (*i.e.* the angular step size of 5.6250° corresponds to ≈ 1.9 mm at the W/poly interface). With improved angular resolution (*e.g.* ≥ 128 images taken over a 360° rotation), we believe that the 2.00 mm features would have been clearly discernable, but the 1.00 mm features are most likely beyond the limits of our current prototype system.

The laboratory research activities described in this section were carried out under the auspices of an approved Integrated Work Sheet (IWS # 10537, *Development of High Energy Neutron Radiography at Ohio University*, RI: J. Hall) and in accordance with all existing OUAL operational and radiation safety guidelines. Copies of these documents and/or additional information on personnel safety issues related to this work may again be obtained directly from the authors of this report upon request.

CONCLUSIONS

The wide variety of unclassified neutron imaging experiments that we have done at OUAL over the past few years using our relatively simple prototype imaging detector, combined with a number of classified Monte Carlo simulations of potential CSA imaging scenarios, have demonstrated the potential effectiveness of high-energy neutron imaging and validated its proposed use as a nonintrusive inspection tool in ESC applications. The design of the RFQ/DTL accelerator system associated with the neutron source is complete and we are making good progress on the development of other key components including the high-pressure "windowless" D_2 gas target endstation and a full-scale prototype of the imaging detector. We are poised to commit to the construction of a full-scale neutron imaging system facility at LLNL when sufficient funds become available (note that procurement of the accelerator system will essentially drive the deployment schedule).

ACKNOWLEDGMENTS

REFERENCES

1. F. Dietrich and J. Hall, "Detector concept for neutron tomography in the 10 - 15 MeV energy range", LLNL doc. UCRL-ID-123490 (LLNL, 1996).
2. F. Dietrich, J. Hall and C. Logan, "Conceptual design for a neutron imaging system for thick target analysis operating in the 10 - 15 MeV energy range," UCRL-JC-124401 (LLNL, 1996), published in *Proc. 14th Int. Conf. on the Application of Accelerators in Research and Industry* (Denton, TX, 1996), AIP **CP392**, ed. J. Duggan and I. Morgan, 837 (1997).
3. J. Hall, F. Dietrich, C. Logan and G Schmid, "Development of high-energy neutron imaging for use in NDE applications", UCRL-JC-134562 (LLNL, 1999), published in *Penetrating Radiation Systems and Applications* (Denver, CO, 1999), SPIE **3769**, ed. F. Doty, 31 (1999).
4. J. Hall, F. Dietrich, C. Logan and B. Rusnak, "Recent Results in the Development of Fast Neutron Imaging Techniques," UCRL-JC-140435 (LLNL, 2000), published in *Proc. 16th Int. Conf. on the Application of Accelerators in Research and Industry* (Denton, TX, 2000), AIP **CP576**, ed. J. Duggan and I. Morgan, 1113 (2001).
5. B. Rusnak and J. Hall, "An accelerator system for neutron radiography," UCRL-JC-139558 (LLNL, 2000), published in *Proc. 16th Int. Conf. on the Applications of Accelerators in Research and Industry* (Denton, TX, 2000), AIP **CP576**, ed. J. L. Duggan and I. L. Morgan, 1105 (2001).
6. J. Hall, "Uncovering hidden defects with neutrons," published in *Science & Technology Review*, May 2001 (LLNL, 2001).
7. R. Hamm, AccSys Technologies, Inc., private communication.
8. E. Iverson, R. Lanza and L. Lidsky, "Windowless gas targets for neutron production," *Proc. 5th Int. Conf. on Neutrons in Research and Industry* (Crete, Greece, 1996), SPIE **2867**, ed. G. Vourvopoulos, 513 (1996).
9. E. Iverson, "Windowless gas targets for neutron production," Ph.D. thesis (unpublished), Massachusetts Institute of Technology, Cambridge, MA, February 1997; R. Lanza, private communication.
10. W. Gerber, "Investigation of windowless gas target systems for particle accelerators," Master's thesis (unpublished), Massachusetts Institute of Technology, Cambridge, MA, June 1998; R. Lanza, private communication.
11. E. Empey, "Implementation of a closed-loop windowless gas target system for neutron production," Master's thesis (unpublished), Massachusetts Institute of Technology, Cambridge, MA, February 2000; R. Lanza, private communication.
12. J. Guzek, *et al*., "Development of High-Pressure Deuterium Gas Targets for the Generation of Intense Monoenergetic Fast Neutron Beams," *Nuclear Instruments and Methods in Physics Research B*, **152**, 512 (1999).
13. D. Schneberk, *et al*., LLNL, "Comparison of 15 MeV and 9 MeV scanning," private communication.

COLLECTED FIGURES
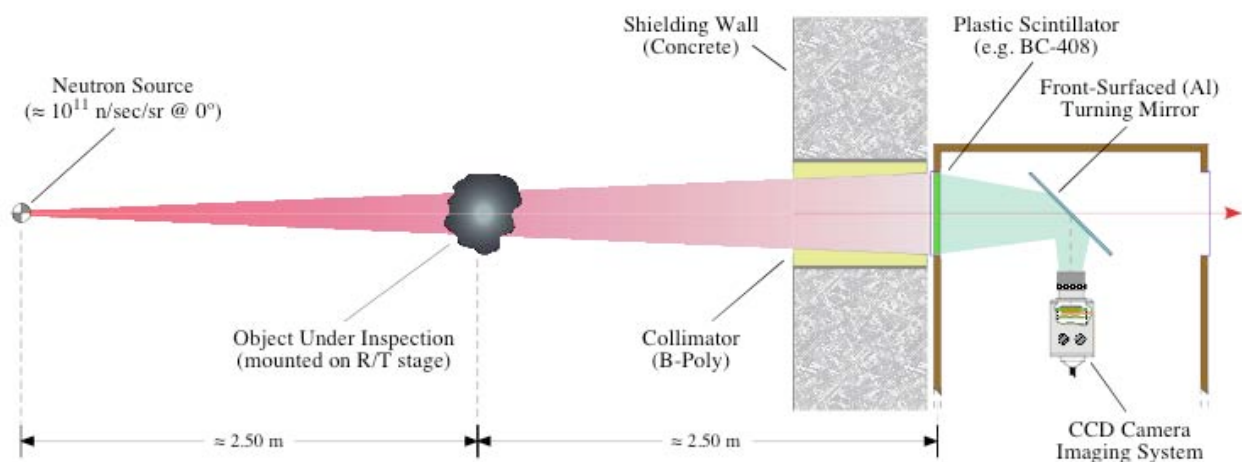
Figure 1: Conceptual design of proposed high-energy neutron imaging system. This particular representation shows the system with a 2:1 image magnification factor (which minimizes image noise caused by internal scattering within the object); however, a magnification factor of 1.25:1 (which offers improved spatial resolution) is also being considered. The objects will be mounted on a rotation/translation stage assembly that will allow either conventional radiographic or full tomographic (CT) imaging.
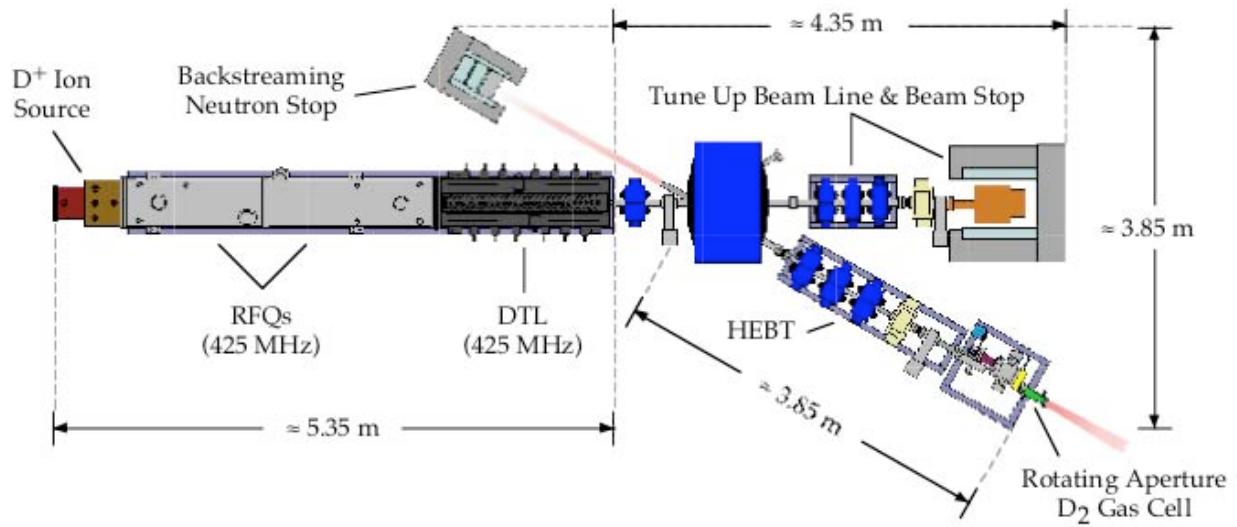
Figure 2: Schematic of proposed high-intensity neutron source. The full-scale, production-line system will consist of a D$^+$ ion source and a pair of compact, radio-frequency quadrupoles (RFQs) coupled to a short drift-tube linac (DTL). The high-energy beam transport (HEBT) system and D$_2$ gas target endstation are also shown along with a tune-up beam line and beam stop.
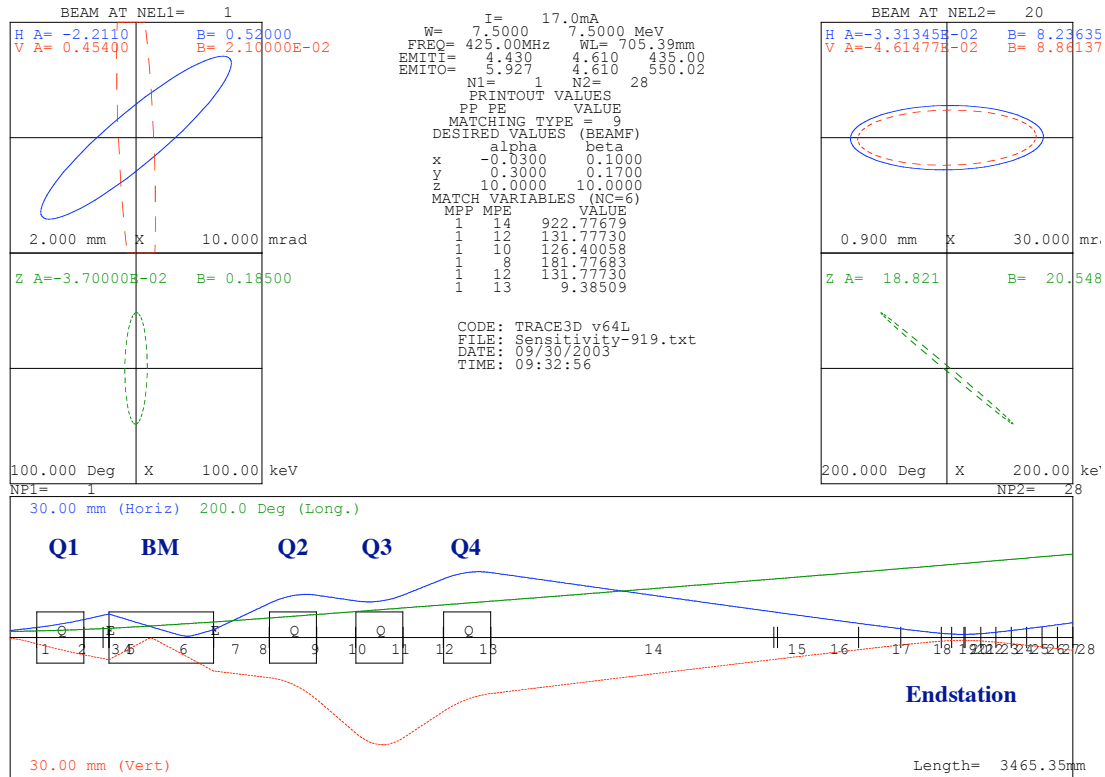

Figure 3: TRACE3D analysis of the conceptual HEBT design showing beam envelopes for $\approx$ 95% transmission through system. A horizontal plot is also shown which shows the relative positions of the first quadrupole, the bending magnet and the final quadrupole triplet designed to focus the beam into the target endstation (waist on the right).
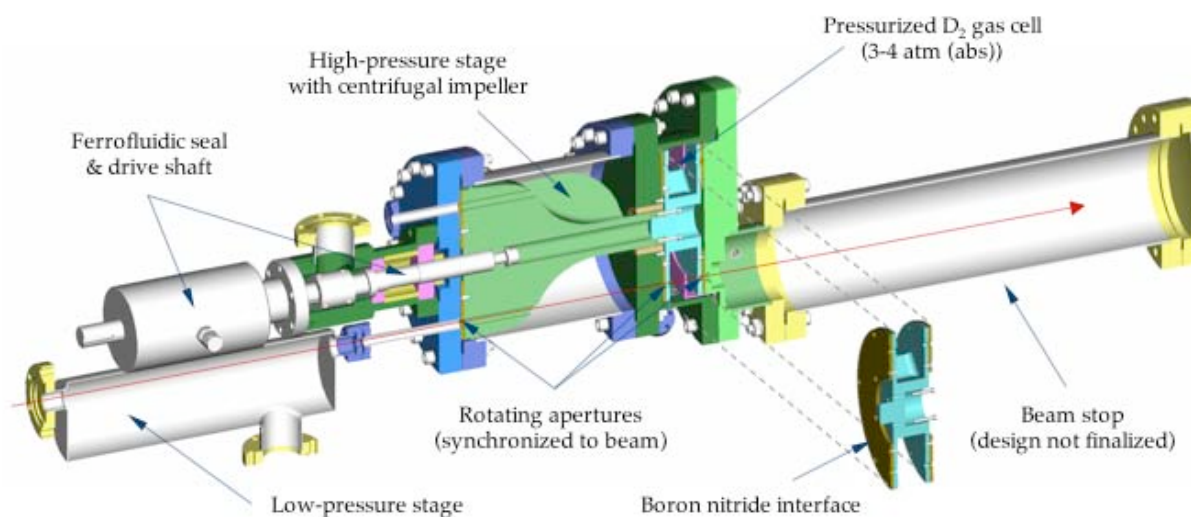
Figure 4: Initial design of "rotating-aperture" D_2 gas target endstation. The high-pressure sealing rotors were immersed in the D_2 target gas in this design to facilitate sealing and minimize pressure-induced pulsing of the rotors; however, the drive motor was located outside of the high-pressure stage which required the use of a Ferrofluidic seal on the vacuum feed-through.
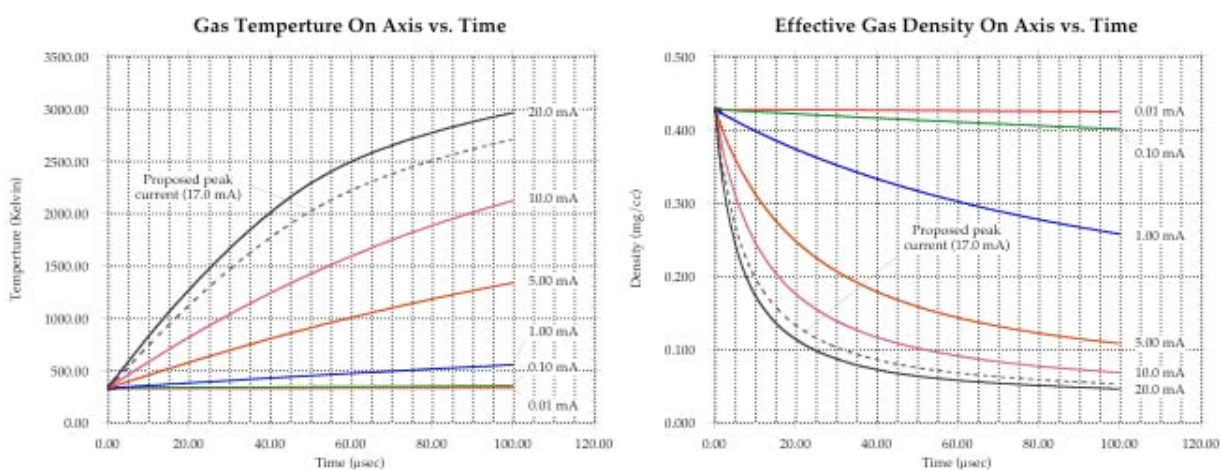
Figure 5: D_2 gas temperature and density vs. time in the beam focus channel for initial endstation design. These results indicated that, for peak beam currents in the 5 - 20 mA range, significant heating of the target gas would occur within 10's of μsec, causing a rapid drop in density along the beam channel ("burn through").
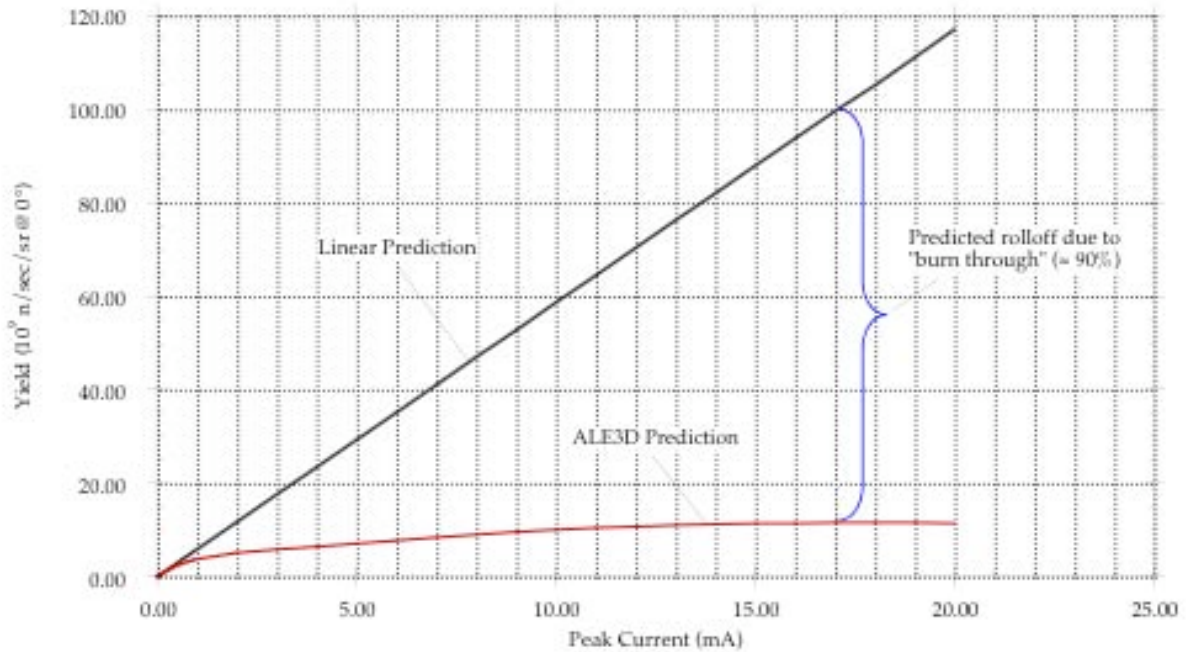
Figure 6: Predicted roll-off (relative to the expected value) in effective neutron yield due to D_2 density rarefactions associated with beam heating. Note that the roll-off for a peak current of ≈ 17 mA (*i.e.* our proposed system) could be $\approx 90\%$ if no measures are taken to mitigate the rarefactions of the D_2 target gas.
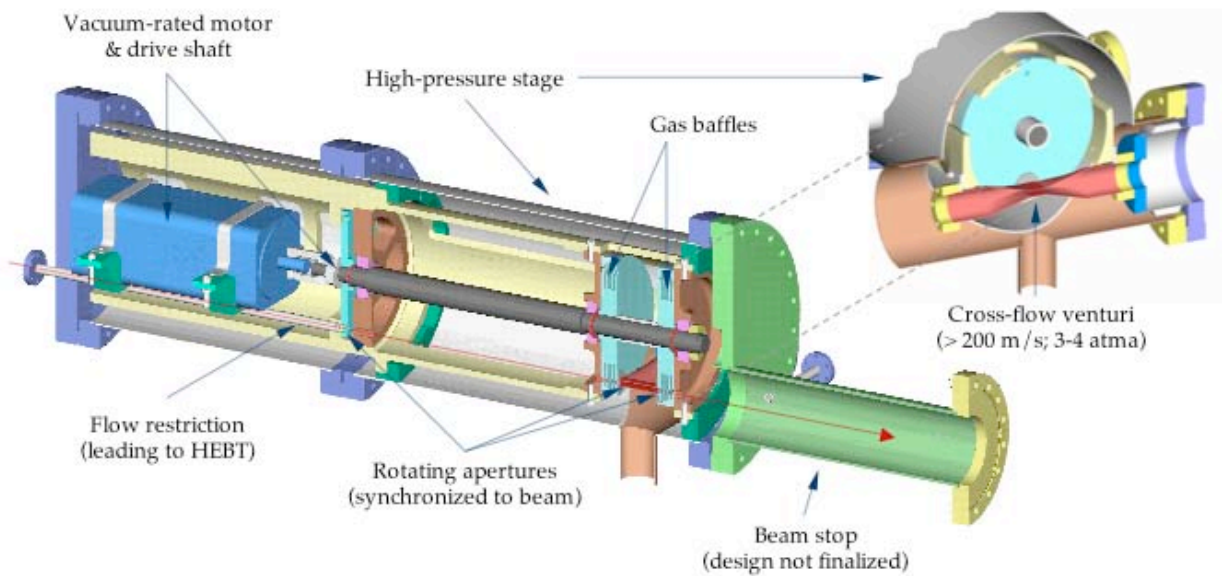
Figure 7: Revised design of "rotating-aperture" D_2 gas target endstation. A cross-flow D_2 venturi capped at either end by baffled, rotating apertures is used in this design to minimize the effect of density rarefactions associated with beam heating.
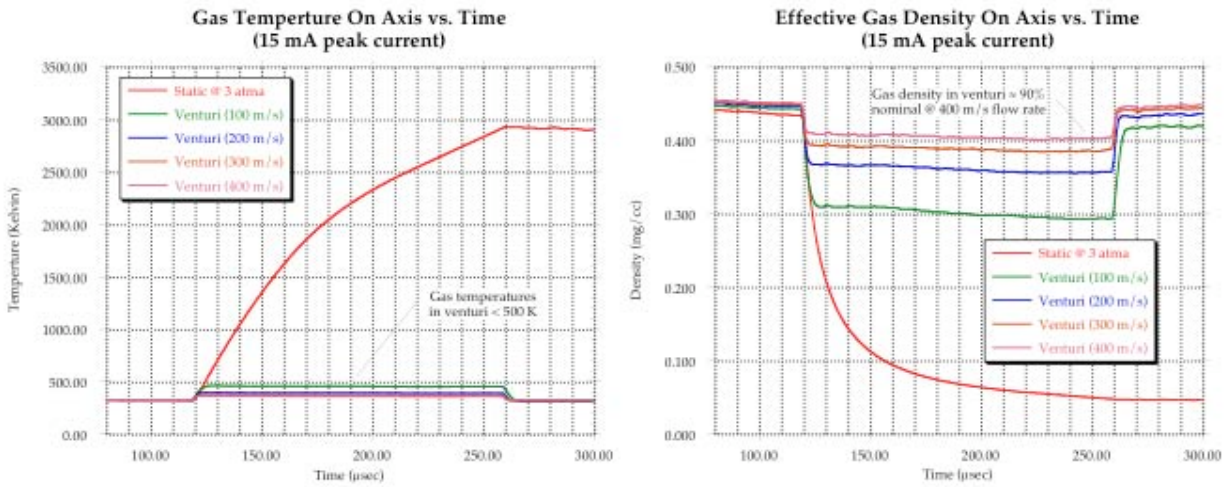
Figure 8: D$_2$ gas temperature and density vs. time in the beam focus channel for revised endstation design. These results indicated that it should be possible to maintain a D$_2$ gas density in the beam channel equivalent to an average pressure of $\approx$ 3 atma using reasonably-sized, commercially-available vacuum pumps and standard gas handling systems.
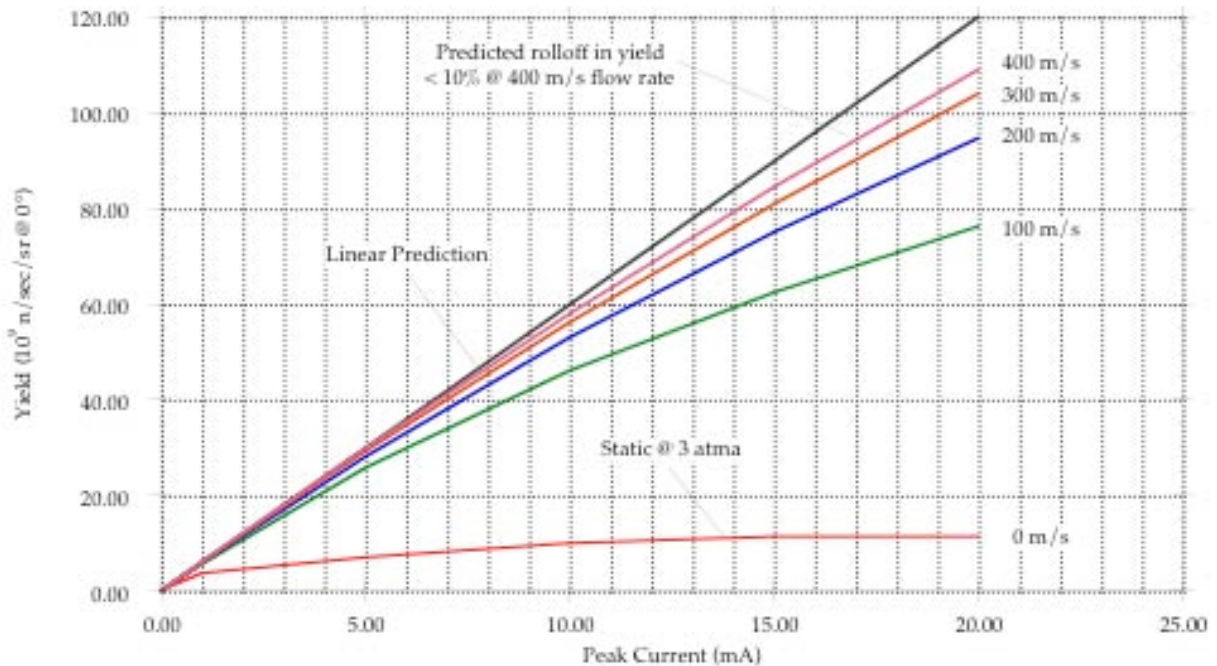
Figure 9: Predicted roll-off (relative to the expected value) in effective neutron yield due to D$_2$ density rarefactions associated with beam heating. Note that the roll-off for a peak current of $\approx$ 17 mA (*i.e.* our proposed system) is now predicted to be < 10% for a venturi gas flow rate of $\approx$ 400 m/s (achievable with our proposed system).

Figure 10: The first of two full-scale prototypes of the new target endstation fabricated by the CHAMP Company of Campbell, CA and delivered to LLNL for use in performance tests. The one-piece, rigid aluminum sub-frame shown here allows us to align and hold the drive motor and all of the various precision parts that need to rotate at $\geq$ 1000 RPM without the need to procure or fabricate special vacuum enclosures that can also be precision aligned.
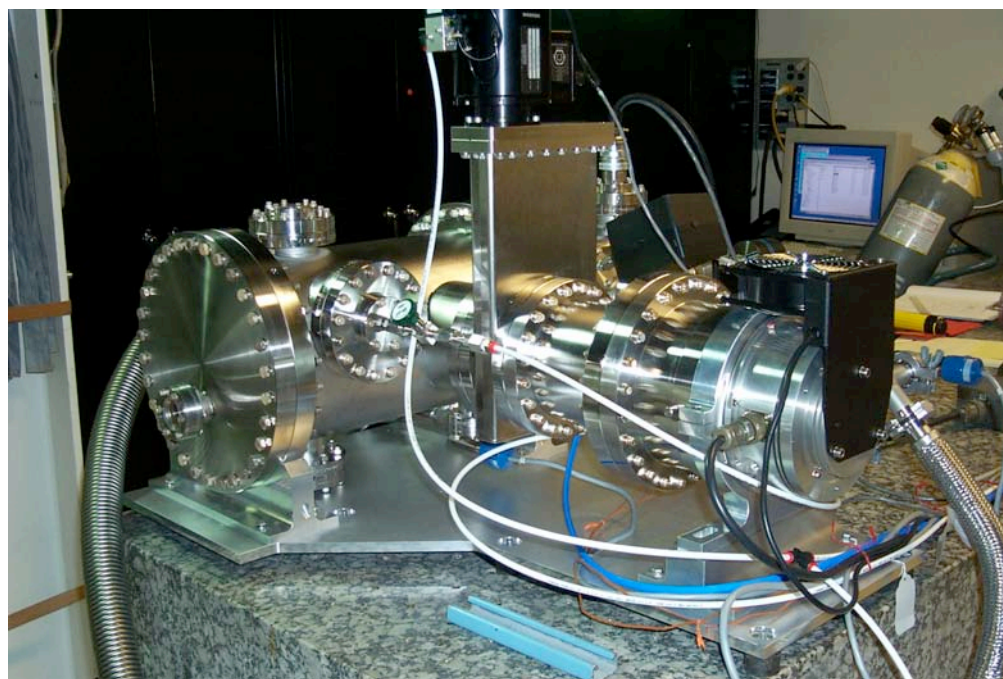
Figure 11: Prototype rotating-aperture endstation assembly installed in custom-designed vacuum enclosure equipped with pumps and diagnostic sensors. Pressure testing of these units was conducted in a shared laboratory space located in B132S.
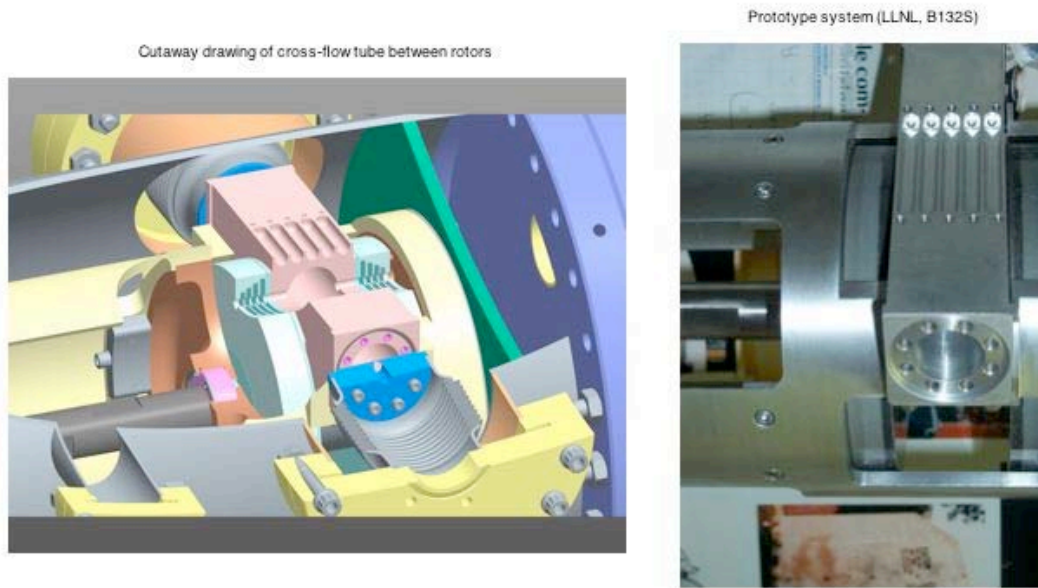
Figure 12: Cutaway drawing and photograph of cross-flow region in endstation flanked by baffled rotors. One of the primary goals in designing and fabricating these initial test units was to verify that we could achieve a gap spacing of ≤ 0.002" between these components. Note that the venturi that would normally be used in an actual production unit has been replaced here by a simple rectangular tube with a straight throat for use in tests with static gas.
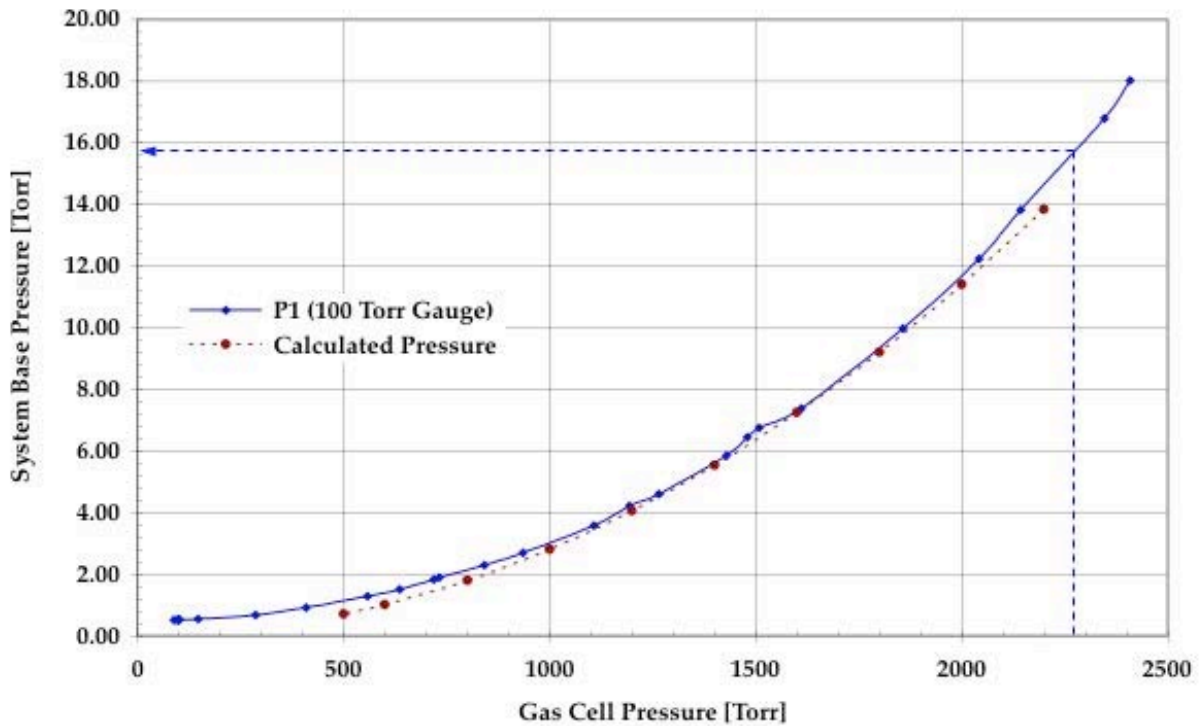
Figure 13: System base pressure vs. gas cell pressure for case of rotors held fixed with apertures misaligned (closed). Gas leakage was limited to the narrow gap between the rotors and stators in this case and was measured to be < 16 Torr when the cross-flow tube was pressurized to ≈ 3 atma (He). Note also that the leak rate was well approximated by theoretical models.
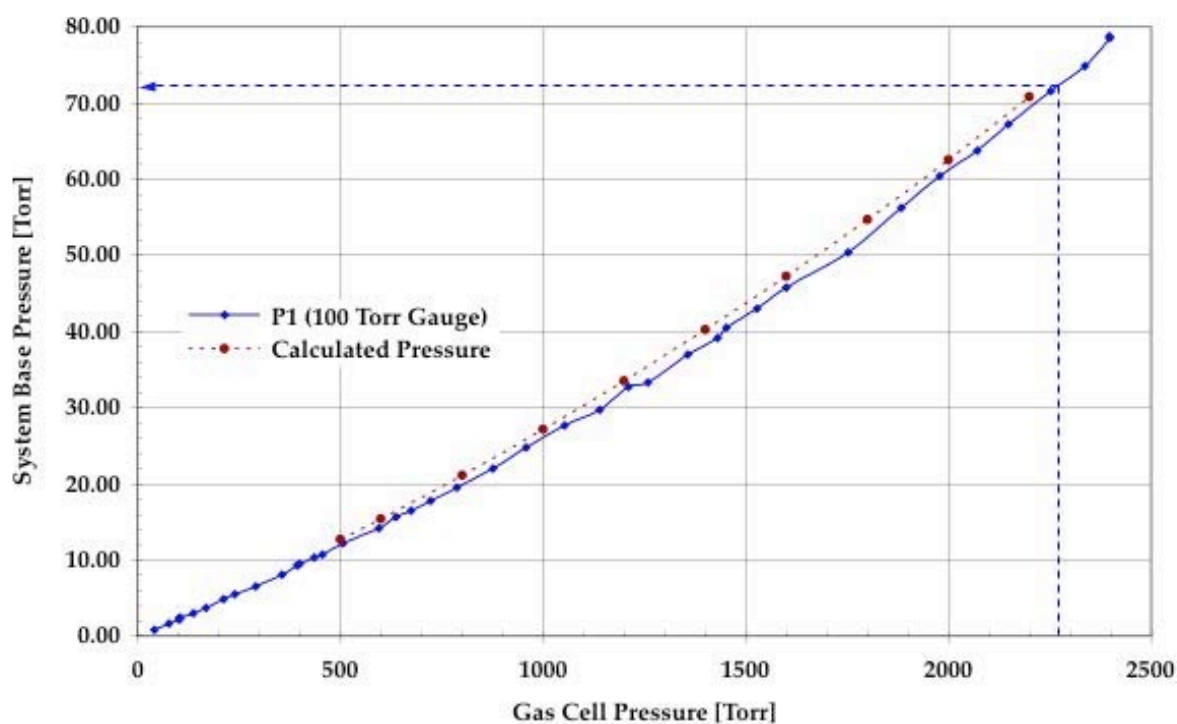
Figure 14: System base pressure vs. gas cell pressure for case of rotors run at typical operating speed ($\approx$ 1000 RPM). The overall leak rate in this case was measured to be < 75 Torr when the cross-flow tube was pressurized to $\approx$ 3 atma (He). Note also that the leak rate was again well approximated by theoretical models.
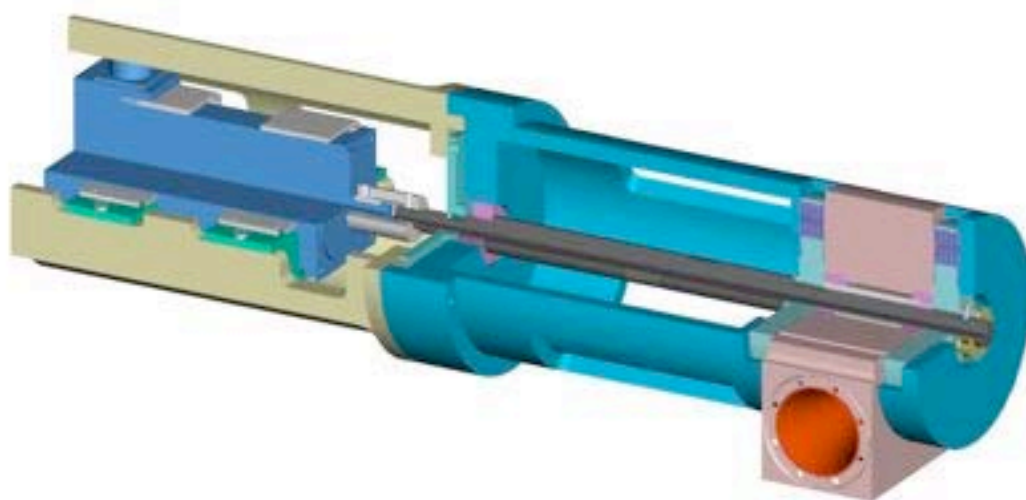
Figure 15: Cutaway drawing of conceptual design of 3rd generation rotating aperture system. This system will use the same drive motor and mounting scheme as our initial RA units, but it will include high-tolerance thrust bearings integrated directly into the block which houses the high-pressure venturi cross-flow tube. We believe that this will allow us to maintain a gap spacing of < 0.001" between the rotors and stators and an overall base pressure in the endstation of < 10 Torr, even when the system is run at high gas pressure ($\geq$ 3 atma).
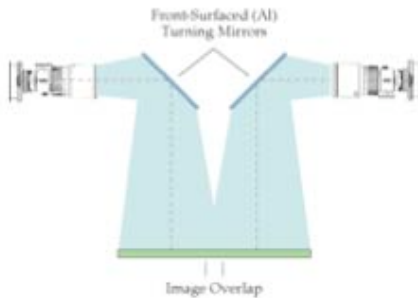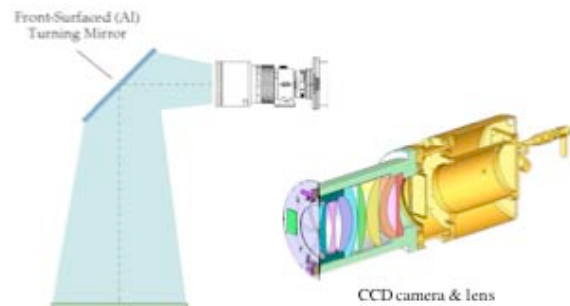
Figure 16: Design options for proposed full-scale imaging detector system. Option 1 (left) is similar to that recently built by Optics1 for use in an ESC high-resolution x-ray imaging system at Pantex (note that image registration would have to be done off line in a secure environment in this case prior to analysis). Option 2 (right) is a much simpler (and lower cost) design similar to that currently being used in our imaging experiments at OUAL. It offers comparable optical resolution to Option 1 and a much higher S/N ratio; however, it is also limited to a somewhat smaller field of view.
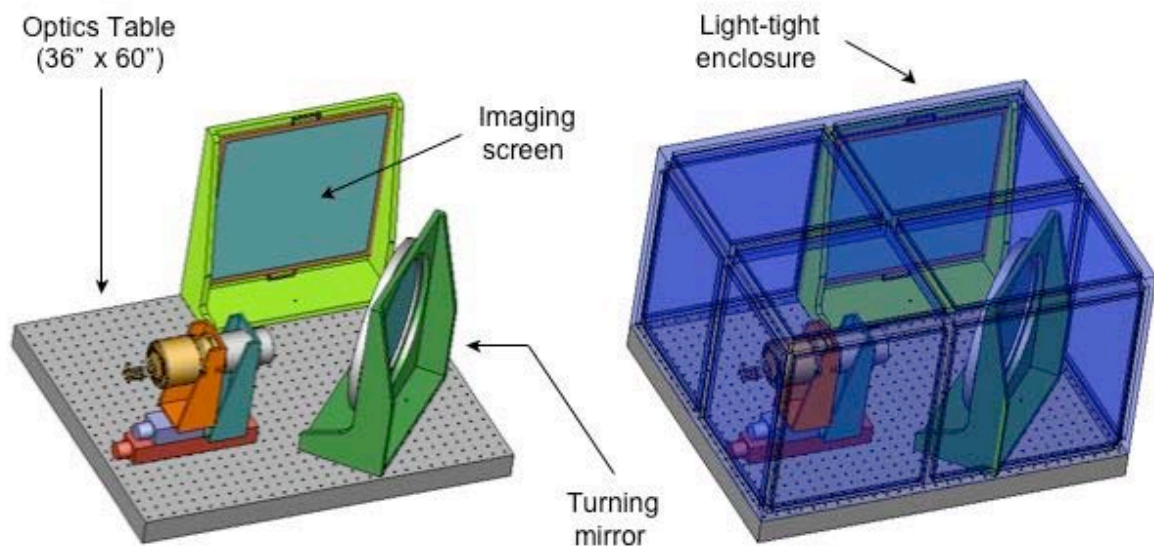
Figure 17: Proposed layout for full-scale prototype of single camera imaging system. The imaging screen in this case would be a thin plastic scintillator ≈ 65 cm X 65 cm and the CCD camera would feature a 4096 X 4096, 15 μm pixel, TE-cooled chip. The ultimate spatial resolution of the system should be ≤ 1.00 mm (FWHM) at the object position.
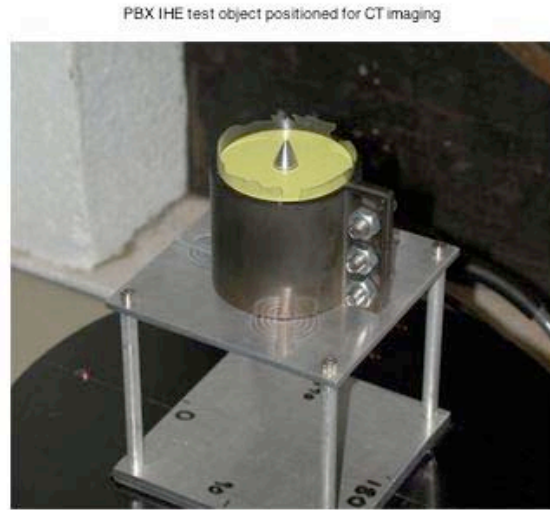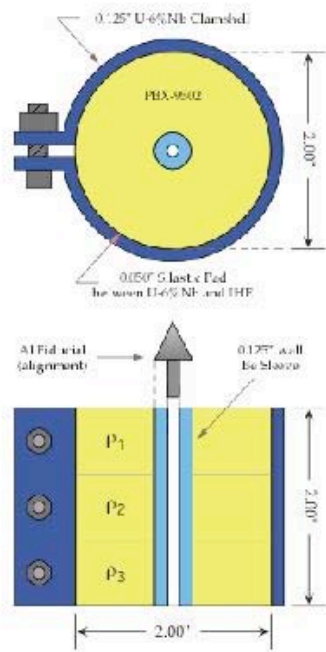
Figure 18: PBX-9502 IHE test object provided by Pantex for use in tomographic (CT) imaging experiments conducted at OUAL during FY04 and FY05. The annular IHE cylinders (compressed to densities that differed by ≤ 0.06 g/cc overall) were bonded together and shielded by a high-Z (U6%Nb) clamshell on the outside and a low-Z (Be) sleeve on the inside.
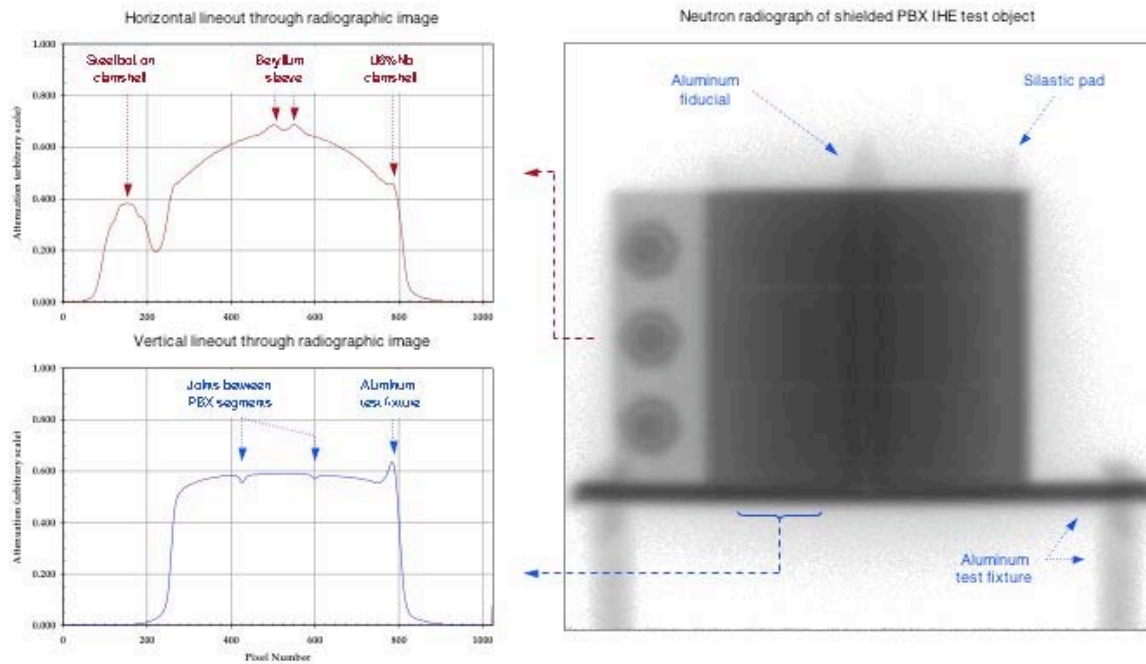

Figure 19: Typical neutron radiograph of Pantex test object. The basic structure of the object, including both outer *and* inner material contours and even the bond joints between the three IHE segments, was clearly discernable in these images. Tomographic (CT) imaging was done using a computer-controlled rotation stage interfaced to our data acquisition system.
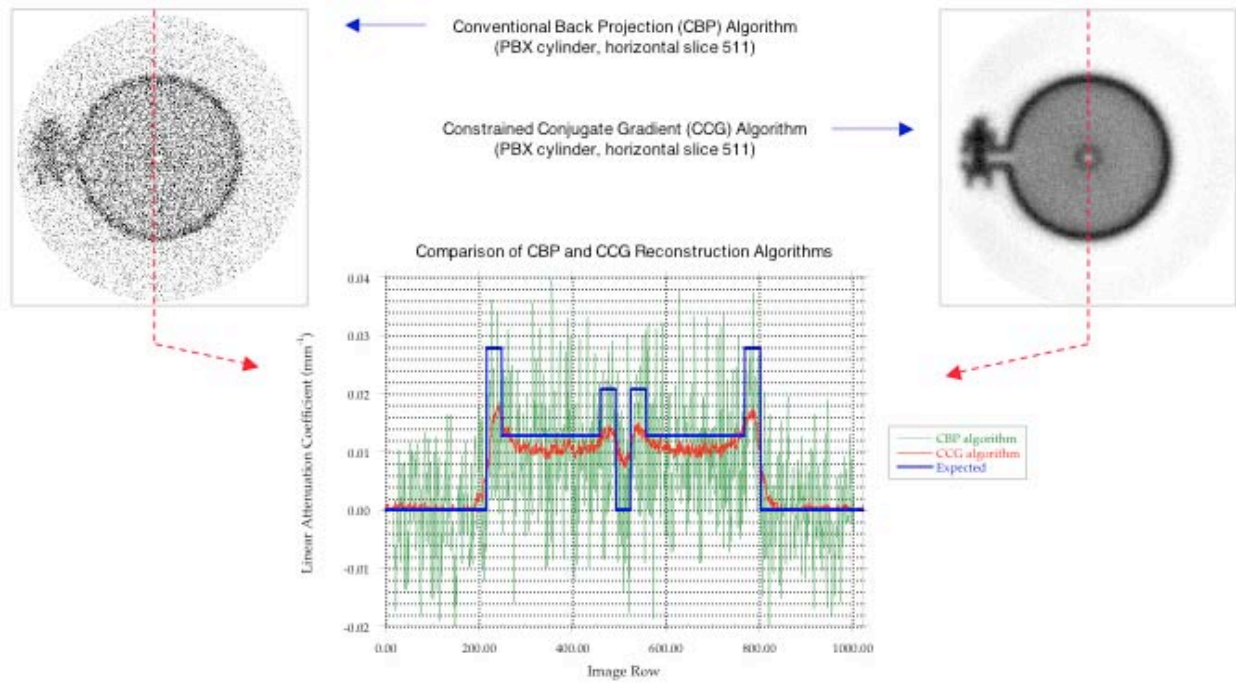
Figure 20: Comparison of Conventional Back Projection (CBP) and Constrained Conjugate Gradient (CCG) tomographic reconstruction algorithms. The CCG algorithm utilizes an iterative, constrained (*e.g.* $\mu X \geq 0$) least-squares fitting procedure which, while somewhat more CPU intensive than CBP, significantly reduces the overall statistical noise level in CT reconstructions. All of the neutron CT data presented in this report were processed using the CCG algorithm.
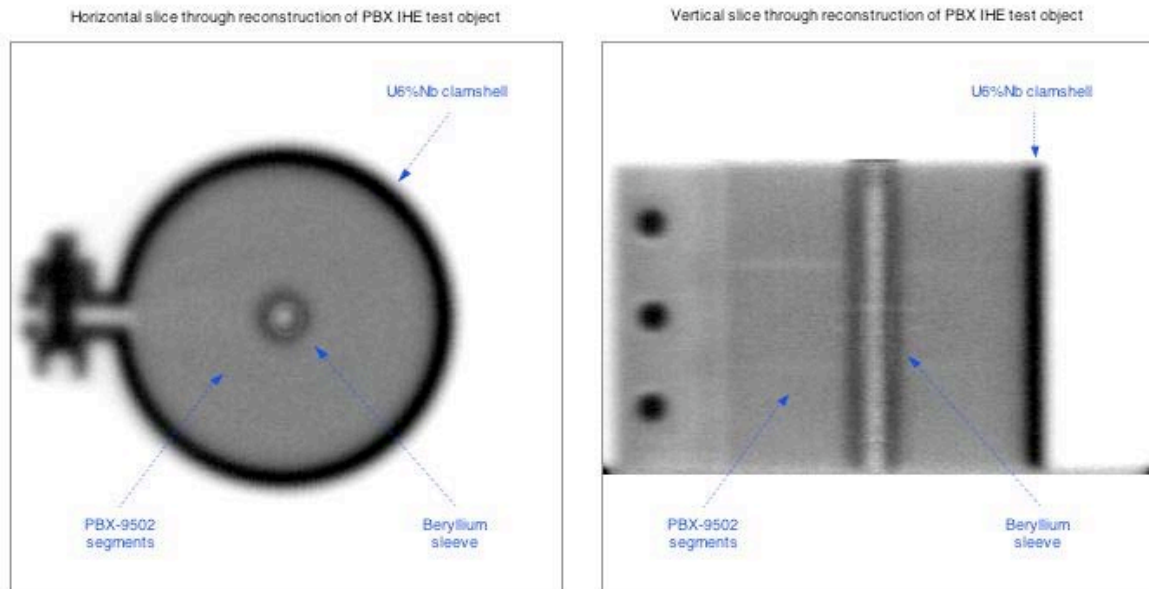

Figure 21: Tomographic reconstructions of Pantex test object. The reconstructions again revealed the basic structure of the object, including outer *and* inner material contours and even the bond joints between the three IHE segments. Several artifacts were also noted in the reconstructions (light colored rings or bands near the center of the images). These were caused by a series of minor scratches in the surface of the plastic scintillator used for imaging in this case.
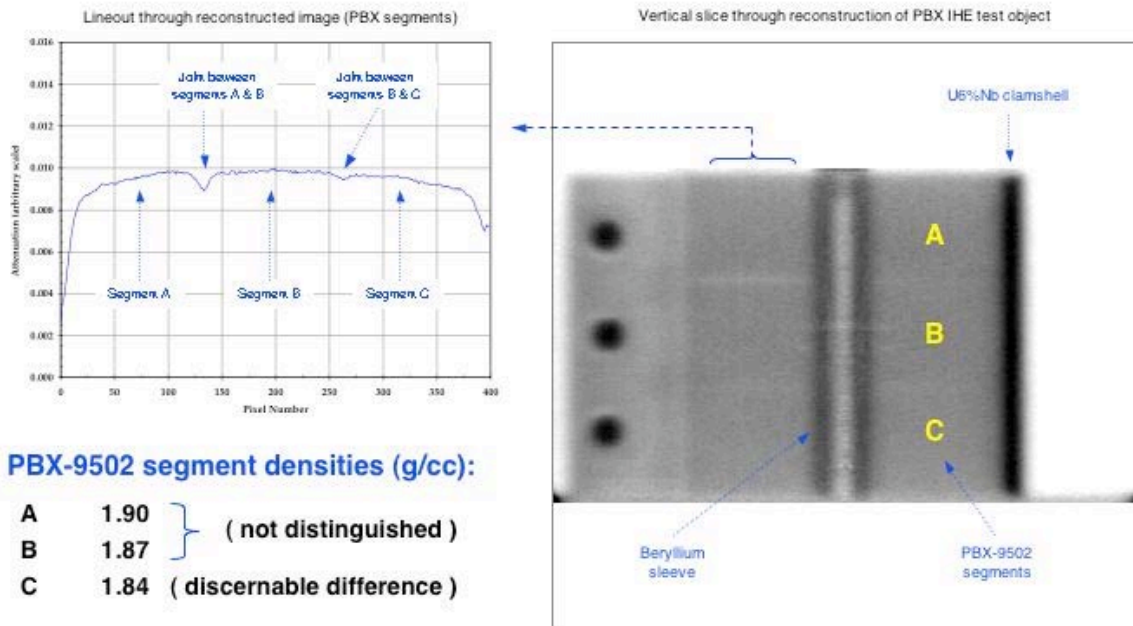
Figure 22: Tomographic reconstruction of Pantex test object (vertical slice at 0˚). In spite of increasing the number of images of the object taken during this run compared to previous experiments (FY04), the small density differences between the IHE segments (≈ 0.03 g/cc) and the holes in the 0.050" Silastic pad were still not clearly discernable in the reconstruction.
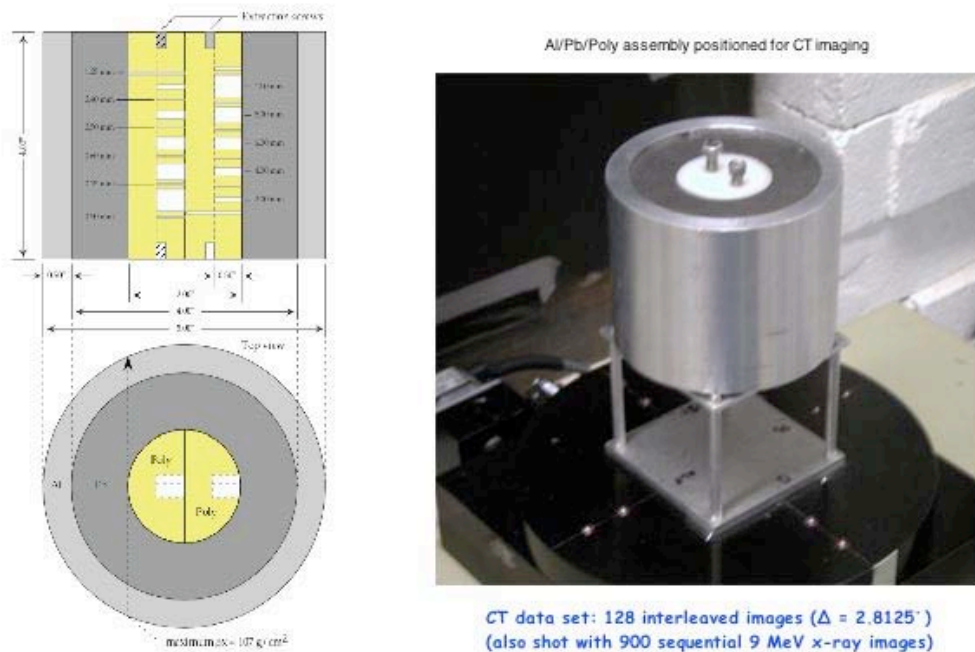

Figure 23: Al/Pb/Poly test object used in neutron tomographic (CT) imaging experiments conducted at OUAL and 9 MeV and 15 MeV x-ray CT imaging experiments conducted at LLNL and Hill AFB, respectively. The poly cylinder at the center actually consisted of two "half cylinders" with a series of 11 holes of different diameters machined into the inner (flat) surface of one half and the outer (curved) surface of the other. The maximum value of ρx for this object (measured along the inner radius of the Pb shell) was estimated to be ≈ 107 gm/cm^2.
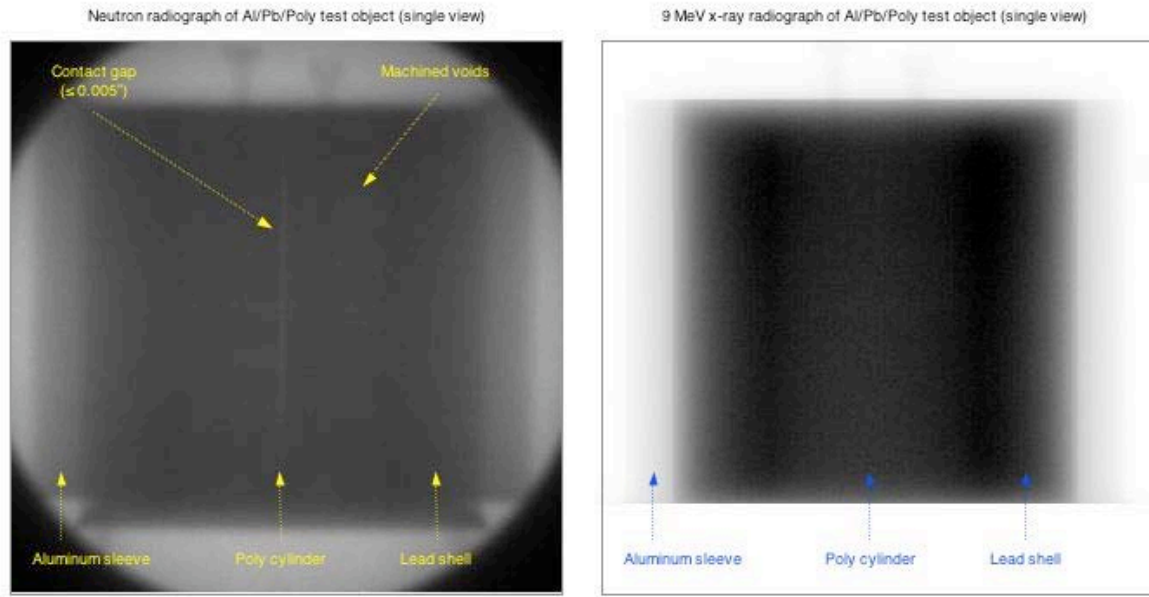
Figure 24: Typical 10 MeV neutron and 9 MeV x-ray radiographs of Al/Pb/Poly test object. The basic structure of the object, including outer material contours and internal voids, was discernable in both cases; however, the individual neutron images showed significantly higher contrast and revealed much greater structural detail (*e.g.* the narrow (≤ 0.005") "contact gap" between the two halves of the poly cylinder) than did the individual x-ray images.
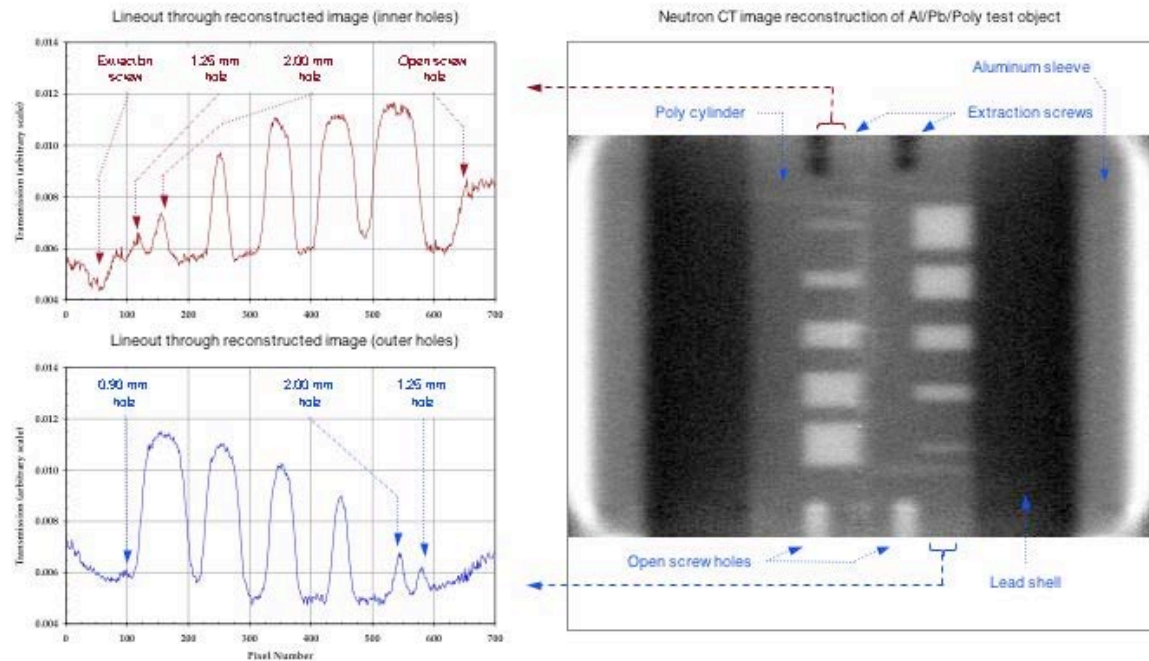

Figure 25: Neutron tomographic reconstruction of Al/Pb/Poly test object (vertical slice at 0°). The detailed shell structure of the object, including both outer *and* inner material contours, extraction screws, open screw holes and voids in the poly cylinder as small as ≈ 1.25 mm in diameter were clearly discernable in the reconstruction. Lineouts taken through the reconstruction revealed even finer details such as the presence of the 0.90 mm diameter hole machined into the outer (curved) surface of the poly half cylinder near the top on the right hand side of this image.
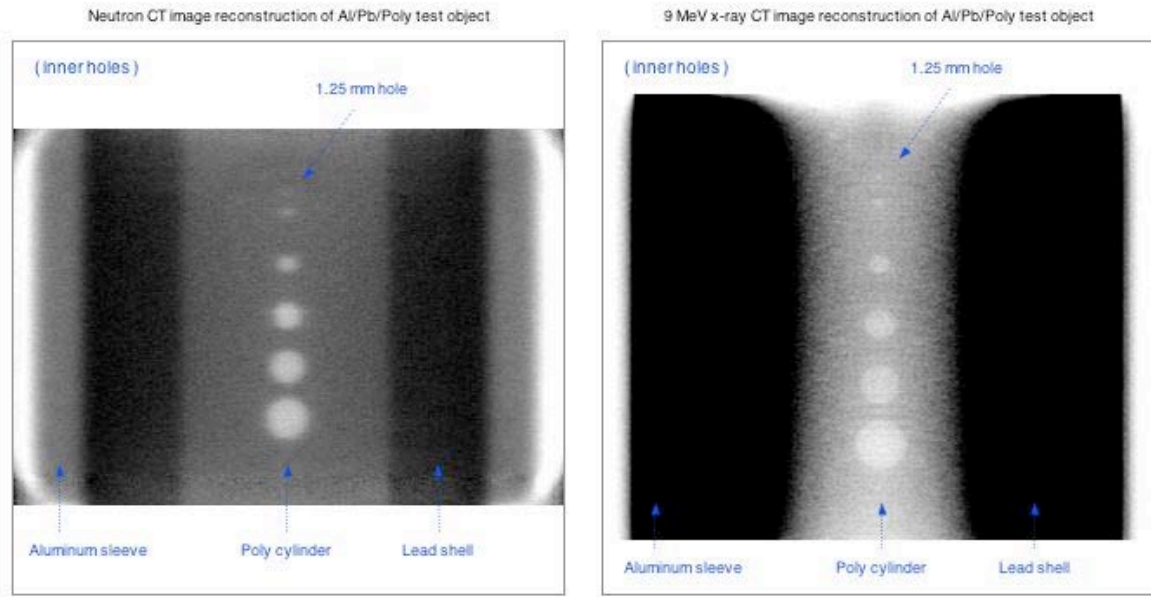
Figure 26: Comparison of 10 MeV neutron and 9 MeV x-ray tomographic reconstructions of Al/Pb/Poly test object (off-axis vertical slices at 90˚). The larger voids (≥ 1.25 mm diameter) near the center of the poly cylinder were clearly discernable in both the neutron and x-ray CT reconstructions; however, the neutron images again showed much higher contrast, allowing the full structure of the test object (*e.g.* voids *and* material contours) to be viewed at a single contrast setting (the contrast in the x-ray image has been adjusted down to the bottom 3% of its range in this case to make the voids visible).
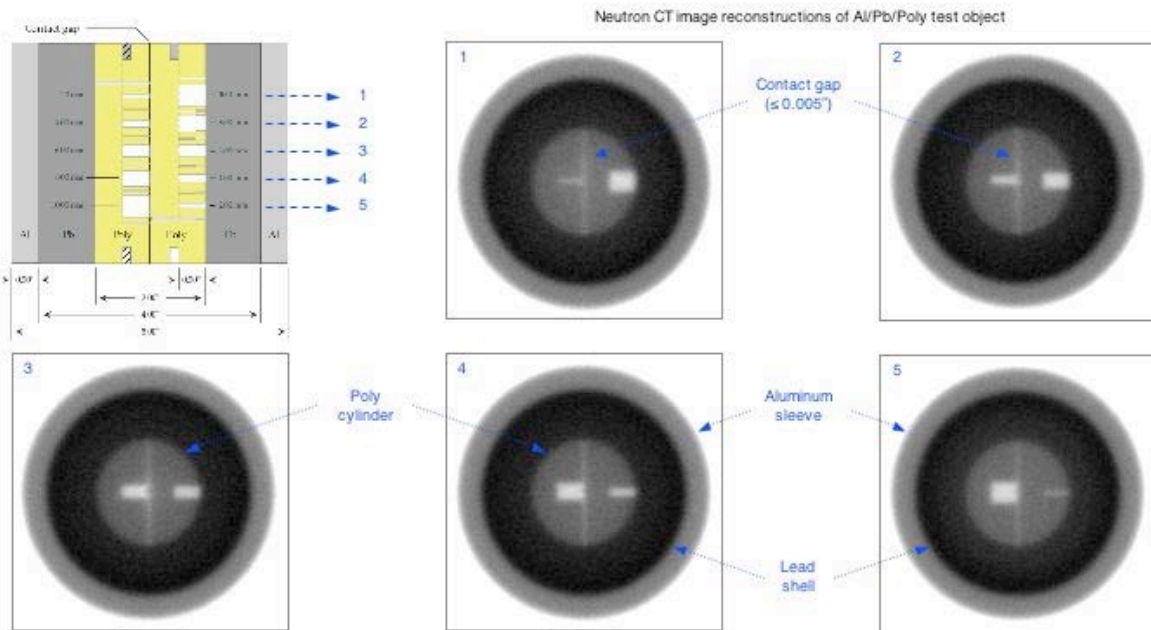

Figure 27: Neutron tomographic reconstruction of Al/Pb/Poly test object (horizontal slices taken at different elevations). Outer *and* inner material contours, machined void structures in the test object and even the narrow (≤ 0.005") "contact gap" between the two halves of the poly cylinder were clearly discernable in the reconstruction (note that, based on our earlier experience imaging this test object, the contact gap does *not* have to be aligned with a viewing angle to be detected).
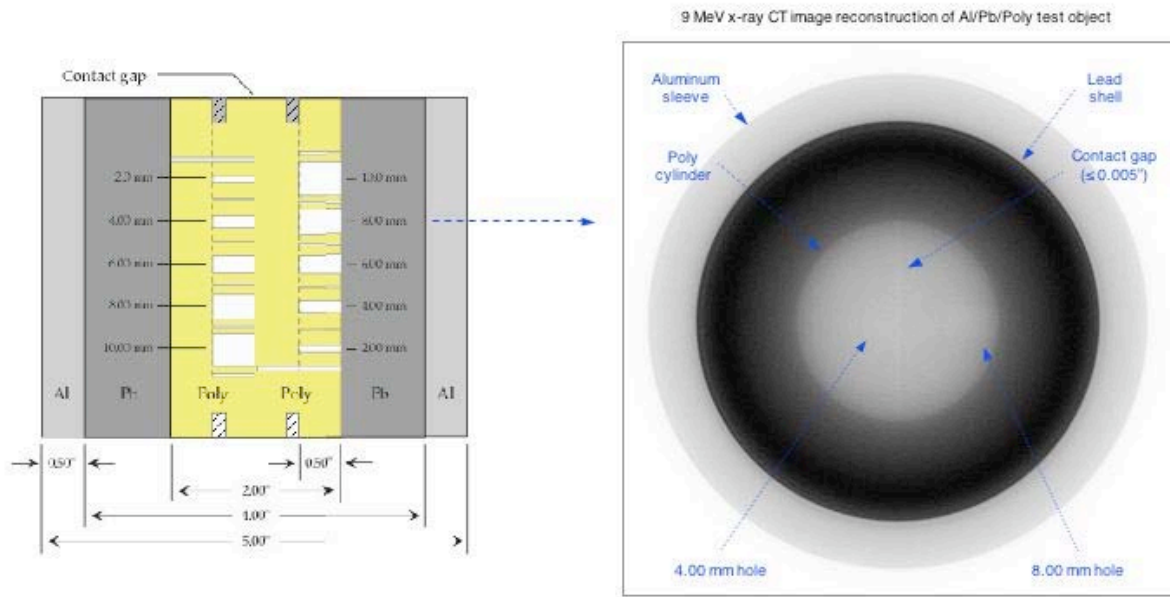
Figure 28: 9 MeV x-ray tomographic reconstruction of Al/Pb/Poly test object (horizontal slice taken at elevation 2). Material contours, the void structures at elevation 2 and the contact gap between the two halves of the poly cylinder were also discernable in the x-ray CT reconstruction, although (again) at *much* lower contrast than in the neutron CT reconstruction. In fairness, however, note also that the spatial resolution in the x-ray reconstruction is better than that for neutrons. This is not expected and is due primarily to the higher resolving power of the specialized scintillating screen used for x-ray imaging.
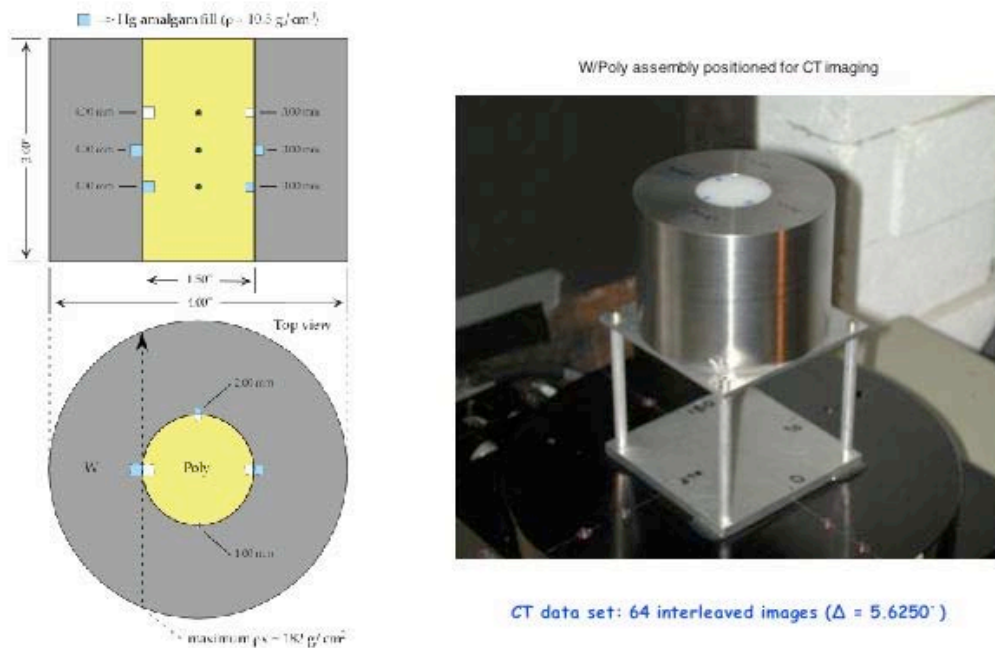

Figure 29: W/Poly test object used in neutron tomographic (CT) imaging experiments conducted at OUAL. Sets of right-circular holes were machined into the inner contour of the W shell at its midplane and the outer contour of the poly cylinder 0.50" above and below its midplane. The holes in the W shell and the lower set of holes in the poly cylinder were then filled with mercury amalgam (dental filling) at a nominal density of ≈ 10.5 g/cc to simulate metal hydride formations. The maximum value of ρx for this object (measured along the inner radius of the W shell) was estimated to be ≈ 182 gm/cm^2.
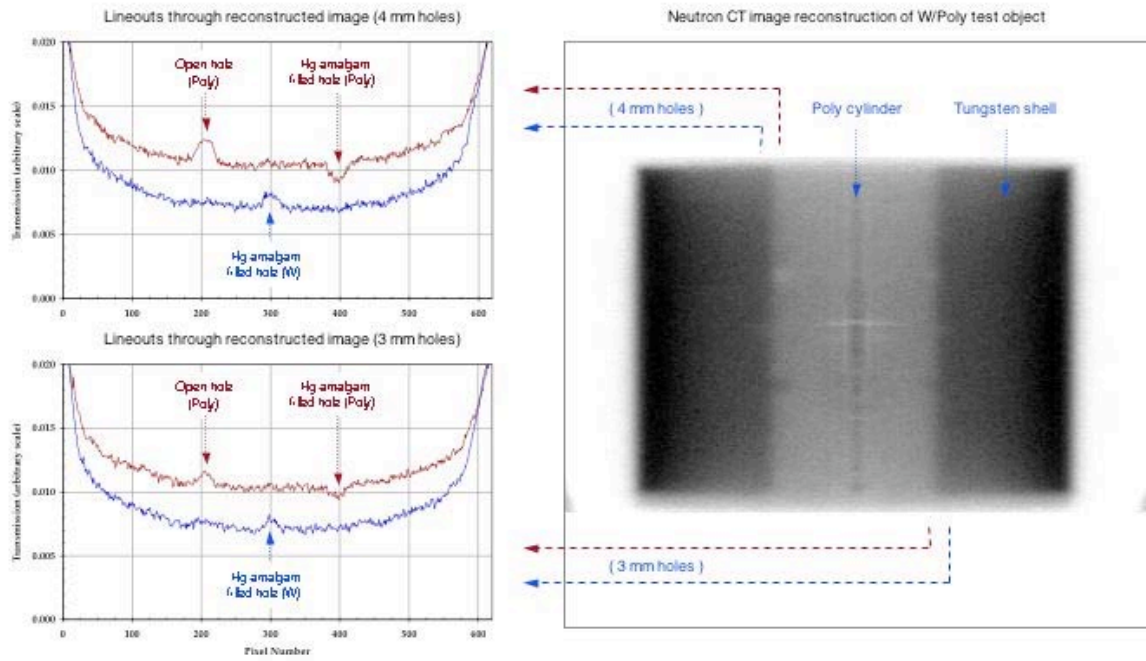
Figure 30: Tomographic reconstruction of W/Poly test object (vertical slice at 0˚). The 4.00 mm (50.3 mm^3) and 3.00 mm (21.2 mm^3) voids and simulated hydride formations in both the poly cylinder and the W shell were clearly discernable in the reconstruction. Several artifacts associated with defects in the scintillator were again noted in the reconstructions.
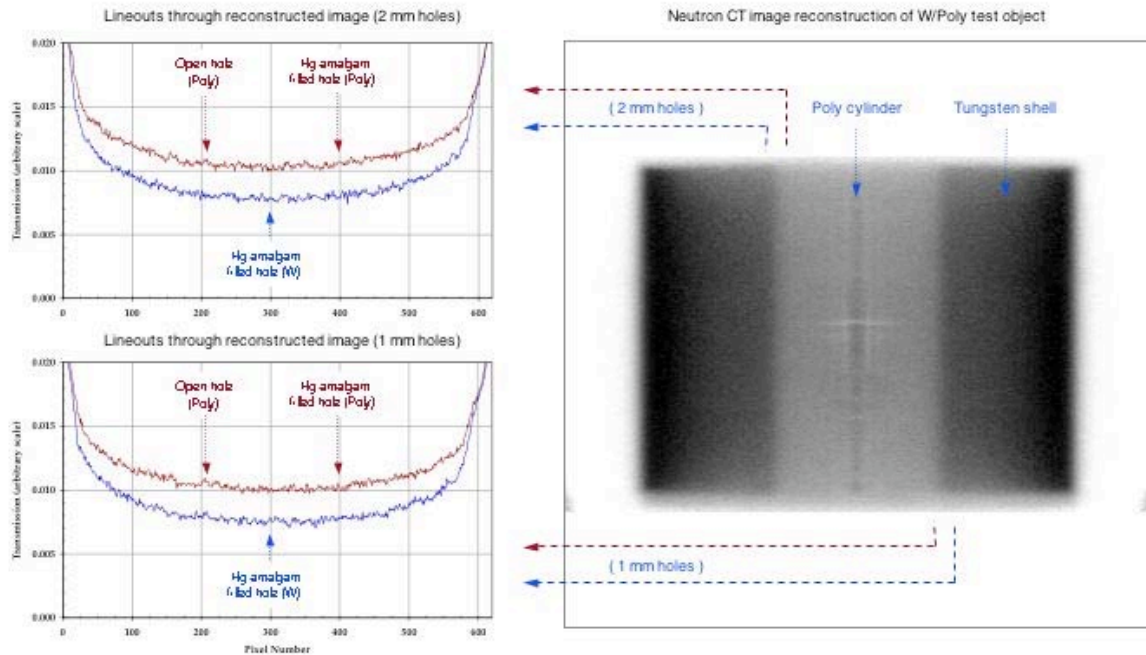

Figure 31: Tomographic reconstruction of W/Poly test object (vertical slice at 90˚). Neither the 2.00 mm (6.28 mm^3) nor the 1.00 mm (0.79 mm^3) features were discernable in the reconstruction due to inadequate angular resolution. With improved angular resolution (*e.g.* ≥ 128 images taken over a 360˚ rotation), we believe that the 2.00 mm features would have been clearly discernable, but the 1.00 mm features are most likely beyond the limits of our current prototype system.